International Journal of Mechanical Sciences 303 (2025) 110569

Contents lists available at ScienceDirect

International Journal of Mechanical Sciences

journal homepage: www.elsevier.com/locate/ijmecsci

Coupling approaches in chemo-mechanical multiphase-field models

Thea Kannenberg [a,b,*], Andreas Prahs [c], Bob Svendsen [d,e], Britta Nestler [a,b,c], Daniel Schneider [a,b]

[a] Karlsruhe Institute of Technology (KIT), Institute for Applied Materials (IAM-MMS), Straße am Forum 7, Karlsruhe, 76131, Germany
[b] Karlsruhe University of Applied Sciences, Institute of Digital Materials Science (IDM), Moltkestraße 30, Karlsruhe, 76133, Germany
[c] Karlsruhe Institute of Technology (KIT), Institute of Nanotechnology (INT-MSS), Hermann-von-Helmholtz-Platz 1, Eggenstein-Leopoldshafen, 76344, Germany
[d] Max Planck Institute for Sustainable Materials, Microstructure Physics and Alloy Design, Max–Planck-Straße 1, Düsseldorf, 40237, Germany
[e] RWTH Aachen University, Material Mechanics, Schinkelstraße 2, Aachen, 52062, Germany

ARTICLE INFO

Keywords:
Multiphase-field method
Chemo-mechanical coupling
Stress-driven diffusion
Diffusion-induced stress
Gibbs-Thomson benchmark

ABSTRACT

Owing to their ability to combine various driving forces and their numerically efficient handling of migrating interfaces, multiphase-field models are widely employed in the multiphysics-based modeling and simulation of multiphase systems in materials science. Chemo-mechanically coupled phenomena, such as stress-driven diffusion and diffusion-induced stresses, are of high interest in various fields including battery materials research and metals. This work discusses the impact of the chemo-mechanical coupling approach on equilibrium states, phase evolution, and component diffusion. To this end, a fully coupled multiphase-field model is derived that accounts for balance equations on singular surfaces and the Hadamard jump conditions. Consequently, mechanical compatibility and chemical equilibrium are ensured in both bulk and interface regions. Furthermore, a scheme is presented that facilitates a direct comparison of the chemo-mechanically fully coupled model with a one-sided and a weakly coupled model. The proposed scheme enables a comparison with sharp interface calculations that are derived from the generalized Gibbs-Thomson equation. Additionally, this scheme is employed as a benchmark to validate the proposed model. Moreover, it is demonstrated that only a model that employs a full chemo-mechanical coupling is capable of capturing stress-driven diffusion as well as diffusion-induced stress.

1. Introduction

A comprehensive understanding of microstructural mechanisms in materials and the corresponding microstructure mechanics is essential for the effective control of these mechanisms. An underlying objective in computational materials science is to optimize material properties while reducing costs and improving sustainability. The coupled modeling of multi-physical processes is an ongoing task in materials science. Stress-assisted diffusion and diffusion-induced stresses are two phenomena that require chemo-mechanical coupling. These phenomena play an important role in a variety of disciplines, including but not limited to the study of battery materials [1,2], the modeling of hydrogen embrittlement [3], and research in the field of steel production [4].

Based on seminal works [5–7], the phase-field method has become a widely used technique for modeling microstructure evolution. In order to circumvent the computational expense associated with interface tracking, interfaces are described by smooth transition zones of finite width. Consequently, interfaces do not generate mathematical discontinuities, instead, phases are associated with order parameters that vary smoothly, cf., e.g., [8–10]. The terminology *phase* is employed in the thermodynamic sense. However, its usage is further expanded to differentiate between distinct grains in polycrystalline materials. The position of the interfaces is implicitly given by the field of order parameters. The combination of various driving forces to model multi-physical problems is a straightforward process. Thus, the phase-field model has emerged as a powerful tool in various applications across materials sciences, e.g., [11–13]. Recent research employs the phase-field method, e.g., to investigate battery materials [14–16], solid state dewetting [17,18], transformation in steels [19,20], additive manufacturing [21,22], and fracture [23–25]. One of the original applications of phase-field methods was solidification, cf., e.g., [26], a field that remains a subject of active research [27,28]. For such applications, the incorporation of concentration fields into phase-field formulations is necessitated. An approach is given by Wheeler, Boettinger, and McFadden (WBM), where a single concentration field c is considered for each species [29]. Thus, for each phase α, equal concentrations are assumed in the interface, i.e., $c^\alpha = c\ \forall\alpha$. Alternatively, equal diffusion

* Corresponding author at: Karlsruhe University of Applied Sciences, Institute of Digital Materials Science (IDM), Moltkestraße 30, Karlsruhe, 76133, Germany.
E-mail addresses: thea.kannenberg@h-ka.de (T. Kannenberg), daniel.schneider@kit.edu (D. Schneider).

https://doi.org/10.1016/j.ijmecsci.2025.110569
Received 20 March 2025; Received in revised form 4 June 2025; Accepted 1 July 2025
Available online 26 July 2025

potentials can be assumed in the interface $\mu^\alpha = \mu \; \forall \alpha$, as proposed in the Kim-Kim-Suzuki (KKS) model [30] or similarly by Tiaden et al. [31]. These formulations are based on the Helmholtz free energy density. Similarly, Plapp [32] and Choudhury and Nestler [33] proposed a formulation based on the grand chemical potential (GCP) density. While, the WBM models intrinsically couple the concentration field to the interface width, the KKS and GCP models decouple the concentration and the interface width, avoiding excess energy within the diffuse interface region. A number of approaches have been put forth to incorporate mechanical driving forces into phase-field methods. The diffuse interface region is the subject of differing assumptions regarding mechanical fields, akin to the introduction of chemical fields. The Voigt-Taylor (VT) approximation, cf., e.g., [34] assumes equal strains, while the Reuss-Sachs (RS) approximation, cf., e.g., [34] assumes equal stresses in the diffuse interface region. The Khachaturyan (KHA) assumption [35] employs interpolation of the eigenstrains and the stiffness tensors. Furthermore, the interpolation scheme introduced by Steinbach and Apel [36] (SA) is equal to RS with equal stresses in the interface and interpolated elastic strains, resulting in an interpolated compliance tensor. This model was applied to the study of pearlitic transformation [37]. Studies have shown [38–40], that the utilization of VT, RS, KHA, and SA interpolation schemes results in excess energy contributions within the diffuse interface area. Consequently, sharp interface (SI) solutions are not reproducible, thereby fostering the development of alternate model formulations that are consistent with SI theory, cf., e.g., [41]. Durga et al. [39,42] suggested a model that ensures both mechanical equilibrium and kinematic compatibility. Applications include, e.g., the growth of intermetallic compounds including elasto-plastic effects [43]. Similarly, Mosler et al. [40] proposed a homogenization method based on partial rank-one relaxation, which was later included in a numerical convergence study [44]. Schneider et al. [38,45,46] introduced a homogenization scheme consistent with SI jump conditions. This is applied, e.g., to simulate martensitic phase transformation [47], the growth of Widmanstätten ferrite [48], and the autocatalytic growth of bainite [49]. Moreover, it was recently combined with crack propagation models [50] and adapted to two phase flow [51].

The work at hand focuses on the coupling of stress and concentration fields in so-called chemo-mechanically coupled phase-field models. In order to develop a comprehensive understanding of the chemo-mechanical phase-field methods, it is imperative to differentiate between the various approaches to coupling. The coupling approach provides a concept for understanding the nature or degree of interaction between different fields. In the field of thermo-mechanics, a detailed discussion on coupling is provided by Prahs et al. [52,53]. Larché and Cahn [54,55] established a theoretical foundation for the study of chemo-mechanical coupling effects by conducting an in-depth analysis of the thermochemical equilibrium of solids under stress, cf. [56]. Svendsen et al. [57] proposed a general framework for the formulation of chemo-mechanical phase-field models in the context of continuum thermodynamics and mixture theory. In the present work, coupling approaches are distinguished as follows:

- A chemo-mechanically fully coupled (CMFC) model is characterized by a mutually dependent balance of linear momentum and diffusion equation. In this case, the stress depends on the concentration field and mechanical contributions are considered in the diffusion equation. The evolution of phases is governed by mechanical and chemical driving forces.
- In contrast, employing a chemo-mechanically weakly coupled (CMWC) model, no mechanical contributions are considered in the diffusion equation and the linear momentum balance does not depend on the concentration field. However, the concentration and stress fields are coupled through the evolution of phases, which is driven by both mechanical and chemical forces.
- Furthermore, a chemo-mechanically one-sided coupled (CMOC) model is taken into consideration, where the linear momentum balance depends on the concentration, while no coupling contributions are accounted for in the diffusion equation. Phase evolution is driven by mechanical and chemical forces.

While the majority of literature on chemo-mechanical phase-field methods does not provide a precise discussion or comparison of the impact of coupling approaches, the importance of coupling is widely acknowledged. Nevertheless, a comprehensive scheme for comparison remains to be developed. CMWC models are widely employed, e.g. [4,48,58,59]. Possible limitations of the GCP model due to its need for explicitly invertible expressions between the diffusion potential and the phase-specific concentrations are discussed, cf., e.g., by Simon et al. [59]. The challenges associated with phase-field methods become particularly evident in the context of coupling due to the necessity of formulating and resolving balance equations within the diffuse interface framework to recover SI solutions. Several works employ CMFC models. For instance Steinbach and Apel [36,37] address a CMFC model employing an SA interpolation scheme. However, the impact of excess energy in the diffuse interface is not discussed. Kamachali et al. [60,61] acknowledge the significance of chemo-mechanical coupling and incorporate concentration-dependent stiffness tensors into their model. However, balance equations on singular surfaces are not accounted for. Furthermore, their analytical solution for the concentration field does not consider all mechanical contributions, making it unsuitable for validating the model with simultaneous phase transformation, diffusion, and mechanical equilibrium calculations. Similarly, Böttger et al. [56] highlight that chemo-mechanical coupling effects cannot be neglected in the context of rafting in Ni-based superalloys. However, balance equations on singular surfaces have not been taken into consideration. Chatterjee et al. [62,63] propose a CMFC model based on a partial rank-one homogenization scheme. This model ensures mechanical compatibility and chemical equilibrium in the diffuse interface region. However, comparison to analytical solutions is only provided for the case of constant and zero eigenstrains, where concentration-dependent elastic fields are not present. Consequently, the presented examples are insufficient to discuss the impact of the chemo-mechanical coupling approach and it remains unclear which effects can be attributed to the full coupling. Furthermore, several works address concentration-dependent mechanical energy densities within a Cahn-Hillard type framework [5]. Within this framework, the concentration field functions as the order parameter, thereby inherently coupling phase transformation and diffusion [64–66]. For instance, Shanthraj et al. [64] propose an algorithmic formulation of CMFC models based on the diffusion potential μ as an independent variable. However, their investigation does not include a comparison of coupling approaches in the diffuse interface context. It should be noted that Cahn-Hillard type models are not included in the comparison presented in this work and, as such, are beyond the scope of this study. A comparison in the field of spinodal decomposition is discussed, e.g., in [67].

The objective of the work at hand is to elucidate how simulated microstructures, e.g., phase transformation, component concentrations, and mechanical equilibrium, are affected by the choice of the chemo-mechanical coupling strategy. In this regard, a scheme is developed, that facilitates the concise comparison of the impact of chemo-mechanical coupling approaches. That scheme can be utilized as a benchmark for model validation, as demonstrated on a novel CMFC phase-field model.

A novel multiphase-field method for two components that is chemo-mechanically fully coupled is derived based on SI balance equations and jump conditions ensuring mechanical compatibility and chemical equilibrium. The comparison scheme, that is developed within this work, highlights the impact of chemo-mechanical coupling approaches on phase transformation, diffusion, and mechanical equilibrium calculations. The single inclusion benchmark setup, which was proposed

Table 1
Frequently used abbreviations.

CMWC	Chemo-mechanically weakly coupled
CMOC	Chemo-mechanically one-sided coupled
CMFC	Chemo-mechanically fully coupled
PFS	Phase-field simulation
SI	Sharp interface

for CMWC phase-field models in a previous work [68], is extended to consider CMFC phase-field models with concentration-dependent eigenstrains. The proposed extended benchmark is suitable to compare the coupling approaches analytically in order to distinguish the impact of weak, one-sided, and full coupling. Analytical SI solutions are derived based on the generalized Gibbs-Thomson equation and used for comparison of the impact of coupling approaches. This setup enables the precise distinction between effects originating from weak, one-sided, and full coupling. Moreover, this setup can be employed for validation of chemo-mechanically coupled phase-field models. Additionally, an illustrative quasi one-dimensional example focusing on transformation kinetics is presented. Furthermore, an illustrative polycrystalline example in two and three dimensions is presented which highlights the mechanical contributions to the diffusion equation inherent in the CMFC model in contrasting juxtaposition to the CMOC and CMWC models. It is shown, that only a CMFC model is capable of capturing stress-induced diffusion and diffusion-induced stress through the incorporation of concentration-dependent strains. In conclusion, criteria for an appropriate coupling approach are presented.

This work is organized as follows. The CMFC model is derived in Section 2. In Section 3.1, the coupling approaches are discussed theoretically and in Section 3.2, analytical solutions for the comparison scheme and benchmark setup are delineated. In Section 4, the coupling approaches are compared using the presented scheme, which is then used as a benchmark to validate the proposed model. Furthermore, illustrative examples evaluating phase transformation kinetics and component diffusion are presented. Finally, this work is concluded in Section 5 with some closing remarks.

In the work at hand, a direct tensor notation is used. Thus, scalars, vectors, 2nd-order, and 4th-order tensors are written as a, $\boldsymbol{a}$, $\boldsymbol{A}$, and $\mathbb{A}$ respectively. A linear mapping of a vector by a tensor of 2nd order reads $\boldsymbol{Ab}$, while a mapping of a tensor of 2nd-order by a tensor of 4th order is written as $\mathbb{A}[\boldsymbol{B}]$. Scalar products are written as $\boldsymbol{a}\cdot\boldsymbol{b}$, $\boldsymbol{A}\cdot\boldsymbol{B}$, and $\mathbb{A}\cdot\mathbb{B}$ and compositions as $\boldsymbol{AB}$ and $\mathbb{AB}$. A dyadic product operator is denoted by $\otimes$. The material time derivative of a field a is denoted by $\dot{a}$. The gradient of a scalar is expressed with the Nabla operator as ∇a. The jump of a quantity ψ with corresponding limits ψ^+ and ψ^- on each side of a material singular surface is written as $\{\psi\} = \psi^+ - \psi^-$. In the phase-field context, it is defined analogously as $\{\psi\}^{\alpha\beta} = \psi^\alpha - \psi^\beta$. The most frequently used abbreviations are summarized in Table 1.

2. Model formulation

In this section, a chemo-mechanically fully coupled multiphase-field model for two components is derived in detail. Within the diffuse interface region, balance equations and the Hadamard jump conditions are accounted for.

2.1. Chemo-mechanically fully coupled multiphase-field model accounting for jump conditions

The modeling and simulation of isothermal chemo-mechanical transformation processes is achieved by employing a two-component multiphase-field model. The free energy functional of Ginzburg–Landau type [6] is expressed as

$$\mathcal{F}[\boldsymbol{\phi},\bar{c},\boldsymbol{u}] = \int_{\mathcal{V}} f_{\text{intf}}(\boldsymbol{\phi},\nabla\boldsymbol{\phi}) + \bar{f}_{\text{chem}}(\boldsymbol{\phi},\bar{c}) + \bar{f}_{\text{el}}(\boldsymbol{\phi},\bar{c},\operatorname{grad}(\boldsymbol{u}))\,\mathrm{d}v \tag{1}$$

and comprises an interfacial f_{intf}, a chemical $\bar{f}_{\text{chem}}$, and a mechanical free energy density $\bar{f}_{\text{mech}}$. Each phase α is associated with a continuous order parameter ϕ_α. All order parameters are accounted for by an N-tuple $\boldsymbol{\phi} = \{\phi_1,\dots,\phi_N\}$. An order parameter assumes the value of 1 within its assigned region and the value of 0 outside of it. Between phases the order parameters vary continuously in the range of $[0,1]$, i.e., in the diffuse interface region at least two phases coexist. The order parameters are constrained by

$$\sum_{\alpha=1}^{N}\phi_\alpha = 1\,, \tag{2}$$

cf., e.g., [69]. The gradients of the N order parameters $\nabla\phi_\alpha$ are written as $\nabla\boldsymbol{\phi} = \{\nabla\phi_1,\dots,\nabla\phi_N\}$. A two-component system, with components A and B is described by the corresponding molar fractions $\bar{c}_{\text{A}}$ and $\bar{c}_{\text{B}}$, which sum up to one, i.e., $\bar{c}_{\text{A}} + \bar{c}_{\text{B}} = 1$. Consequently, the formulation reduces to one independent concentration variable $\bar{c}$, with $\bar{c}_{\text{A}} = \bar{c}$ and $\bar{c}_{\text{B}} = 1 - \bar{c}$. The concentration $\bar{c}$ is defined by interpolation of the phase-specific concentrations c^α, i.e.,

$$\bar{c} = \sum_{\alpha=1}^{N}\phi_\alpha c^\alpha\,. \tag{3}$$

Herein, one independent phase-specific concentration variable c^α is considered with $c^\alpha_{\text{A}} = c^\alpha$ and $c^\alpha_{\text{B}} = 1 - c^\alpha$. The interface energy density f_{intf} is additively composed of a multi-obstacle potential energy density

$$f_{\text{pot}}(\boldsymbol{\phi}) = \frac{16}{\epsilon\pi^2}\sum_{\beta=2}^{N}\sum_{\alpha=1}^{\beta-1}\gamma_{\alpha\beta}\phi_\alpha\phi_\beta\,, \tag{4}$$

cf., e.g., [69] and a gradient energy density

$$f_{\text{grad}}(\nabla\boldsymbol{\phi}) = -\epsilon\sum_{\beta=2}^{N}\sum_{\alpha=1}^{\beta-1}\gamma_{\alpha\beta}\nabla\phi_\alpha\cdot\nabla\phi_\beta\,, \tag{5}$$

as proposed in [70], i.e., $f_{\text{intf}} = f_{\text{pot}} + f_{\text{grad}}$. Herein, $\gamma_{\alpha\beta}$ refers to the interfacial energy between phases α and β and is assumed to be isotropic. The parameter ϵ is related to the width of the interface in equilibrium l_{eq} through $l_{\text{eq}} = \epsilon\pi^2/4$. The multi-obstacle potential is set to ∞ if $\boldsymbol{\phi}$ is not within the Gibbs simplex $\mathcal{G} = \{\boldsymbol{\phi} : \sum_{\alpha=1}^{N}\phi_\alpha = 1, \phi_\alpha \geq 0\}$. By interpolation of the phase-specific chemical free energy densities f^α_{chem} the chemical free energy density $\bar{f}_{\text{chem}}$ is obtained as

$$\bar{f}_{\text{chem}}(\boldsymbol{\phi},\bar{c}) = \sum_{\alpha=1}^{N}\phi_\alpha f^\alpha_{\text{chem}}(c^\alpha(\boldsymbol{\phi},\bar{c}))\,. \tag{6}$$

Analogously, the elastic free energy density $\bar{f}_{\text{el}}$ is given by

$$\bar{f}_{\text{el}}(\boldsymbol{\phi},\bar{c},\operatorname{grad}(\boldsymbol{u})) = \sum_{\alpha=1}^{N}\phi_\alpha f^\alpha_{\text{el}}(c^\alpha(\boldsymbol{\phi},\bar{c}),\boldsymbol{\varepsilon}^\alpha(\boldsymbol{\phi},\operatorname{grad}(\boldsymbol{u})))\,. \tag{7}$$

Emphasis is placed on the fact that the elastic energy density $\bar{f}_{\text{el}}$ is modeled not only dependent on the order parameters $\boldsymbol{\phi}$ and the displacement vector $\boldsymbol{u}$ but also on the concentration $\bar{c}$. In this work, a small strain framework is considered, i.e.,

$$\bar{\boldsymbol{\varepsilon}} = \operatorname{sym}(\operatorname{grad}(\boldsymbol{u}))\,, \tag{8}$$

where $\operatorname{sym}(\cdot) = ((\cdot) + (\cdot)^{\mathsf{T}})/2$ denotes the symmetric part of a tensor.

The evolution equation of the corresponding order parameter is computed as the superposition of pairwise interactions of $\tilde{N}$ locally present phases as

$$\dot{\phi}_\alpha = -\frac{1}{\epsilon}\sum_{\beta=1,\beta\neq\alpha}^{\tilde{N}}M_{\alpha\beta}\left(\frac{1}{\tilde{N}}\left(\frac{\delta f_{\text{intf}}}{\delta\phi_\alpha} - \frac{\delta f_{\text{intf}}}{\delta\phi_\beta}\right) + B_{\alpha\beta}\Delta^{\alpha\beta}_{\text{bulk}}\right)\,, \tag{9}$$

cf., e.g., [10]. Hoffrogge et al. [71] found that the choice of the bulk driving force prefactor as $B_{\alpha\beta} = 4(\phi_\alpha + \phi_\beta)/\pi\sqrt{\phi_\alpha\phi_\beta}$ yields the most accurate representation of triple junction movements in comparison

with analytical solutions. In Eq. (9), the mobility of an $\alpha\beta$-interface is denoted by $M_{\alpha\beta}$. Moreover, the variational derivative

$$\frac{\delta}{\delta\phi_\alpha} = \frac{\partial}{\partial\phi_\alpha} - \operatorname{div}\left(\frac{\partial}{\partial\nabla\phi_\alpha}\right), \tag{10}$$

as given in [72, Eq. (13.63)], is employed. It is applied to Eqs. (4)–(5) to derive the interfacial driving force. The bulk driving force $\Delta^{\alpha\beta}_{\text{bulk}}$ is additively composed of a chemical driving force $\Delta^{\alpha\beta}_{\text{chem}} = \left(\delta/\delta\phi_\alpha - \delta/\delta\phi_\beta\right)\bar{f}_{\text{chem}}$ and a mechanical driving force $\Delta^{\alpha\beta}_{\text{mech}} = \left(\delta/\delta\phi_\alpha - \delta/\delta\phi_\beta\right)\bar{f}_{\text{el}}$, given by $\Delta^{\alpha\beta}_{\text{bulk}} = \Delta^{\alpha\beta}_{\text{chem}} + \Delta^{\alpha\beta}_{\text{mech}}$. The derivatives of the mechanical energy densities Eq. (7) with respect to the gradient of the order parameters $\nabla\phi_\alpha$ are disregarded, as done in [45], and thus

$$\Delta^{\alpha\beta}_{\text{bulk}} = \left(\frac{\delta}{\delta\phi_\alpha} - \frac{\delta}{\delta\phi_\beta}\right)\left(\bar{f}_{\text{chem}} + \bar{f}_{\text{el}}\right) = \left(\frac{\partial}{\partial\phi_\alpha} - \frac{\partial}{\partial\phi_\beta}\right)\left(\bar{f}_{\text{chem}} + \bar{f}_{\text{el}}\right) \tag{11}$$

is considered. The derivative of the bulk energy densities with respect to the order parameter ϕ_α yields

$$\frac{\partial(\bar{f}_{\text{chem}} + \bar{f}_{\text{el}})}{\partial\phi_\alpha} = \frac{\partial}{\partial\phi_\alpha}\sum_{\gamma=1}^{\tilde{N}}\phi_\gamma\left(f^\gamma_{\text{chem}} + f^\gamma_{\text{el}}\right) \tag{12}$$

$$= f^\alpha_{\text{chem}} + f^\alpha_{\text{el}} + \sum_{\gamma=1}^{\tilde{N}}\phi_\gamma\left(\frac{\partial f^\gamma_{\text{chem}}}{\partial\phi_\alpha} + \frac{\partial f^\gamma_{\text{el}}}{\partial\phi_\alpha}\right) \tag{13}$$

$$= f^\alpha_{\text{chem}} + f^\alpha_{\text{el}} + \underbrace{\sum_{\gamma=1}^{\tilde{N}}\phi_\gamma\left(\frac{\partial f^\gamma_{\text{chem}}}{\partial c^\gamma} + \frac{\partial f^\gamma_{\text{el}}}{\partial c^\gamma}\right)\frac{\partial c^\gamma}{\partial\phi_\alpha}}_{:=\mathcal{T}_1} + \underbrace{\sum_{\gamma=1}^{\tilde{N}}\phi_\gamma\frac{\partial f^\gamma_{\text{el}}}{\partial\varepsilon^\gamma}\cdot\frac{\partial\varepsilon^\gamma}{\partial\phi_\alpha}}_{:=\mathcal{T}_2}. \tag{14}$$

In order to simplify the term $\mathcal{T}_1$ the diffusion potential μ^α is defined as

$$\mu^\alpha := \frac{\partial f^\alpha_{\text{bulk}}}{\partial c^\alpha} = \frac{\partial f^\alpha_{\text{chem}} + f^\alpha_{\text{el}}}{\partial c^\alpha}. \tag{15}$$

It may be decomposed into two distinct potentials: the chemical diffusion potential μ^α_{chem} and the mechanical diffusion potential μ^α_{el} reading

$$\mu^\alpha_{\text{chem}} = \frac{\partial f^\alpha_{\text{chem}}}{\partial c^\alpha} \quad\text{and}\quad \mu^\alpha_{\text{el}} = \frac{\partial f^\alpha_{\text{el}}}{\partial c^\alpha}. \tag{16}$$

Moreover, the chemo-mechanical diffusion potentials are assumed equal in the interface

$$\mu = \mu^\alpha = \mu^\alpha_{\text{chem}} + \mu^\alpha_{\text{el}} \quad \forall\alpha \in [1, N], \tag{17}$$

as, e.g., in [56,73,74]. As an approximation, molar volumes V_{m} with units $\text{m}^3\,\text{mol}^{-1}$ are considered phase-independent, i.e.,

$$V_{\text{m}} = V^\alpha_{\text{m}} \quad \forall\alpha \in [1, N] \tag{18}$$

is assumed, as often done in the phase-field community, cf., e.g., [75, 76].

Remark. In a two-component system, analogous to the concentration, each component A and B is associated with an individual chemo-mechanical potential $\hat{\mu}_{\text{A}}$ and $\hat{\mu}_{\text{B}}$. The number of independent chemo-mechanical potentials is reduced to one, and a chemo-mechanical potential difference $\mu = \hat{\mu}_{\text{A}} - \hat{\mu}_{\text{B}}$ is considered, referred to as the diffusion potential, cf., e.g., [75, Eq. (9)], [76, p. 5]. Moreover, the diffusion potential μ with units $\text{J}\,\text{m}^{-3}$ is associated with the molar diffusion potential $\tilde{\mu}$ with units $\text{J}\,\text{mol}^{-1}$ through $\mu = \tilde{\mu}/V_{\text{m}}$.

Furthermore, it is considered that $\bar{c}$ and $\boldsymbol{\phi}$ are both governing variables and, thus, independent, i.e., $\partial\bar{c}/\partial\phi_\alpha = 0$. Consequently, with Eq. (3) and $\partial\bar{c}/\partial\phi_\alpha = \sum_{\gamma=1}^{\tilde{N}}\partial(\phi_\gamma c^\gamma)/\partial\phi_\alpha = 0$, it follows

$$-c^\alpha = \sum_{\gamma=1}^{\tilde{N}}\phi_\gamma\frac{\partial c^\gamma}{\partial\phi_\alpha}, \tag{19}$$

cf., e.g., [48], [77, p. 32]. In conclusion, by substituting Eqs. (16)–(19) it follows

$$\begin{aligned}\mathcal{T}_1 &:= \sum_{\gamma=1}^{\tilde{N}}\phi_\gamma\left(\frac{\partial f^\gamma_{\text{el}}}{\partial c^\gamma} + \frac{\partial f^\gamma_{\text{chem}}}{\partial c^\gamma}\right)\frac{\partial c^\gamma}{\partial\phi_\alpha}\\ &= \sum_{\gamma=1}^{\tilde{N}}\phi_\gamma\left(\mu^\gamma_{\text{el}} + \mu^\gamma_{\text{chem}}\right)\frac{\partial c^\gamma}{\partial\phi_\alpha}\\ &= -c^\alpha\mu.\end{aligned} \tag{20}$$

In the subsequent steps, the term $\mathcal{T}_2$, defined in Eq. (14), is simplified. In this work, a jump condition approach, cf., e.g., [39,40,45] is employed. The displacement gradient is defined as $\bar{\boldsymbol{H}} = \operatorname{grad}(\boldsymbol{u})$, with $\boldsymbol{u}$ denoting the displacement field. In the diffuse interface context, the jump condition is given by

$$\llbracket\boldsymbol{H}\rrbracket^{\alpha\beta} = \boldsymbol{a}^{\alpha\beta}\otimes\boldsymbol{n}^{\alpha\beta} \quad\text{with}\quad \llbracket\boldsymbol{H}\rrbracket^{\alpha\beta} = \boldsymbol{H}^\alpha - \boldsymbol{H}^\beta, \tag{21}$$

cf., e.g., [78, Eq. (7)]. Here, $\boldsymbol{a}^{\alpha\beta}$ denotes the unknown jump vector and the normal vector $\boldsymbol{n}^{\alpha\beta}$ is defined as $\boldsymbol{n}^{\alpha\beta} = (\nabla\phi_\alpha - \nabla\phi_\beta)/|\nabla\phi_\alpha - \nabla\phi_\beta|$, cf., e.g., [9]. The displacement gradient $\bar{\boldsymbol{H}}$ is given by an interpolation of the phase-specific displacement gradients, i.e., $\bar{\boldsymbol{H}} = \sum_{\alpha=1}^{\tilde{N}}\phi_\alpha\boldsymbol{H}^\alpha$. Thus, accounting for Eq. (21), the phase-specific displacement gradients $\boldsymbol{H}^\alpha$ can be expressed in terms of the interpolated displacement gradient and the jumps of the phase-specific displacement gradients as

$$\boldsymbol{H}^\beta = \bar{\boldsymbol{H}} - \sum_{\gamma=1,\gamma\neq\beta}^{\tilde{N}}\phi_\gamma\llbracket\boldsymbol{H}\rrbracket^{\gamma\beta} \quad\text{and}\quad \boldsymbol{H}^\beta = \bar{\boldsymbol{H}} + \sum_{\gamma=1,\gamma\neq\beta}^{\tilde{N}}\phi_\gamma\llbracket\boldsymbol{H}\rrbracket^{\beta\gamma}. \tag{22}$$

Moreover, Eq. (22) is reformulated in terms of the strain with $\bar{\boldsymbol{\varepsilon}} = \sum_{\alpha=1}^{\tilde{N}}\phi_\alpha\boldsymbol{\varepsilon}^\alpha$ as

$$\boldsymbol{\varepsilon}^\gamma = \bar{\boldsymbol{\varepsilon}} + \sum_{\delta=1,\delta\neq\gamma}^{\tilde{N}}\phi_\delta\llbracket\boldsymbol{\varepsilon}\rrbracket^{\gamma\delta}, \tag{23}$$

cf., e.g., [78, Eq. (11)]. Thus, the derivation of the phase-specific strains with respect to the order parameters is given by

$$\frac{\partial\boldsymbol{\varepsilon}^\gamma}{\partial\phi_\alpha} = \sum_{\delta=1,\delta\neq\gamma}^{\tilde{N}}\frac{\partial\phi_\delta}{\partial\phi_\alpha}\llbracket\boldsymbol{\varepsilon}\rrbracket^{\gamma\delta} = \llbracket\boldsymbol{\varepsilon}\rrbracket^{\gamma\alpha} \quad \forall\gamma\neq\alpha. \tag{24}$$

The infinitesimal phase-specific strain $\boldsymbol{\varepsilon}^\alpha$ is additively composed of an elastic part $\boldsymbol{\varepsilon}^\alpha_{\text{el}}$, concentration-independent eigenstrains $\tilde{\boldsymbol{\varepsilon}}^\alpha_0$, and concentration-dependent eigenstrains $\tilde{\boldsymbol{\varepsilon}}^\alpha_{\text{c}}$, i.e., $\boldsymbol{\varepsilon}^\alpha = \boldsymbol{\varepsilon}^\alpha_{\text{el}} + \tilde{\boldsymbol{\varepsilon}}^\alpha_0 + \tilde{\boldsymbol{\varepsilon}}^\alpha_{\text{c}}$. Thus, the elastic strain is given by

$$\boldsymbol{\varepsilon}^\alpha_{\text{el}}(\boldsymbol{\phi}, \bar{c}, \operatorname{grad}(\boldsymbol{u})) = \boldsymbol{\varepsilon}^\alpha(\boldsymbol{\phi}, \operatorname{grad}(\boldsymbol{u})) - \tilde{\boldsymbol{\varepsilon}}^\alpha_0 - \tilde{\boldsymbol{\varepsilon}}^\alpha_{\text{c}}(c^\alpha(\boldsymbol{\phi}, \bar{c})). \tag{25}$$

This work focuses on comparing the impact of chemo-mechanical coupling approaches. In order to accentuate the observed effects, no additional influences such as dissipative behavior are superimposed. The reader is referred to [78–80] for the extension of the jump condition approach to include crystal plasticity, which is not considered in the work at hand. The phase-specific elastic energy densities f^α_{el} are defined as

$$f^\alpha_{\text{el}} = \frac{1}{2}(\boldsymbol{\varepsilon}^\alpha - \tilde{\boldsymbol{\varepsilon}}^\alpha_0 - \tilde{\boldsymbol{\varepsilon}}^\alpha_{\text{c}})\cdot\left(\mathbb{C}^\alpha[\boldsymbol{\varepsilon}^\alpha - \tilde{\boldsymbol{\varepsilon}}^\alpha_0 - \tilde{\boldsymbol{\varepsilon}}^\alpha_{\text{c}}]\right), \tag{26}$$

where $\mathbb{C}^\alpha$ defines the phase-specific stiffness tensor, which can be dependent on the concentration c^α. Consequently, the derivative of f^α_{el} with respect to $\boldsymbol{\varepsilon}^\alpha$ yields the phase-specific stress via Hooke's law, reading

$$\frac{\partial f^\alpha_{\text{el}}}{\partial\boldsymbol{\varepsilon}^\alpha} = \mathbb{C}^\alpha[\boldsymbol{\varepsilon}^\alpha - \tilde{\boldsymbol{\varepsilon}}^\alpha_0 - \tilde{\boldsymbol{\varepsilon}}^\alpha_{\text{c}}] = \boldsymbol{\sigma}^\alpha. \tag{27}$$

Herein, the phase-specific Cauchy stress tensor is denoted by $\boldsymbol{\sigma}^\alpha$. By substituting Eq. (24) and (27), term $\mathcal{T}_2$ in Eq. (14) can be simplified as

$$\begin{aligned}\mathcal{T}_2 &:= \sum_{\gamma=1}^{\tilde{N}} \phi_\gamma \frac{\partial f_{\text{el}}^\gamma}{\partial \boldsymbol{\varepsilon}^\gamma} \cdot \frac{\partial \boldsymbol{\varepsilon}^\gamma}{\partial \phi_\alpha} \\ &= \sum_{\gamma=1,\gamma\neq\alpha}^{\tilde{N}} \phi_\gamma \boldsymbol{\sigma}^\gamma \cdot \{\boldsymbol{\varepsilon}\}^{\gamma\alpha} . \end{aligned} \tag{28}$$

Finally, substituting Eq. (20) and (28) in Eq. (14) the bulk driving force $\Delta_{\text{bulk}}^{\alpha\beta}$ defined in Eq. (11) reads

$$\begin{aligned}\Delta_{\text{bulk}}^{\alpha\beta} &= \{f_{\text{el}}\}^{\alpha\beta} + \{f_{\text{chem}}\}^{\alpha\beta} - \mu\{c\}^{\alpha\beta} \\ &\quad + \underbrace{\sum_{\gamma=1,\gamma\neq\alpha}^{\tilde{N}} \phi_\gamma \boldsymbol{\sigma}^\gamma \cdot \{\boldsymbol{\varepsilon}\}^{\gamma\alpha} - \sum_{\gamma=1,\gamma\neq\beta}^{\tilde{N}} \phi_\gamma \boldsymbol{\sigma}^\gamma \cdot \{\boldsymbol{\varepsilon}\}^{\gamma\beta}}_{\mathcal{T}_3} . \end{aligned} \tag{29}$$

The minimization of Eq. (1), with respect to the displacement $\boldsymbol{u}$ yields the quasi-static balance of linear momentum without body forces

$$\operatorname{div}(\bar{\boldsymbol{\sigma}}) = \mathbf{0} , \tag{30}$$

with the definition of the interpolated Cauchy stress $\bar{\boldsymbol{\sigma}}$ as

$$\bar{\boldsymbol{\sigma}} = \sum_{\alpha=1}^{N} \phi_\alpha \boldsymbol{\sigma}^\alpha , \tag{31}$$

cf., e.g., [78, Eq. (14)]. As described in detail in [78, A.2], with $\{\boldsymbol{\varepsilon}\}^{\alpha\beta} = -\{\boldsymbol{\varepsilon}\}^{\beta\alpha}$, the term $\mathcal{T}_3$ is simplified as

$$\mathcal{T}_3 := \sum_{\gamma=1,\gamma\neq\alpha}^{\tilde{N}} \phi_\gamma \boldsymbol{\sigma}^\gamma \cdot \{\boldsymbol{\varepsilon}\}^{\gamma\alpha} - \sum_{\gamma=1,\gamma\neq\beta}^{\tilde{N}} \phi_\gamma \boldsymbol{\sigma}^\gamma \cdot \{\boldsymbol{\varepsilon}\}^{\gamma\beta} \tag{32}$$

$$= \left(\phi_\alpha \boldsymbol{\sigma}^\alpha + \phi_\beta \boldsymbol{\sigma}_\beta\right) \cdot \{\boldsymbol{\varepsilon}\}^{\beta\alpha} + \sum_{\gamma=1,\gamma\neq\alpha,\gamma\neq\beta}^{\tilde{N}} \phi_\gamma \boldsymbol{\sigma}^\gamma \cdot \{\boldsymbol{\varepsilon}\}^{\beta\alpha} \tag{33}$$

$$= \sum_{\gamma=1}^{\tilde{N}} \phi_\gamma \boldsymbol{\sigma}^\gamma \cdot \{\boldsymbol{\varepsilon}\}^{\beta\alpha} \tag{34}$$

$$= \bar{\boldsymbol{\sigma}} \cdot \{\boldsymbol{\varepsilon}\}^{\beta\alpha} . \tag{35}$$

Herein, the symmetry of the stress tensor $\bar{\boldsymbol{\sigma}} = \bar{\boldsymbol{\sigma}}^{\mathsf{T}}$ given by the balance of angular momentum is considered. Finally, the bulk driving force reads

$$\Delta_{\text{bulk}}^{\alpha\beta} = \{f_{\text{el}}\}^{\alpha\beta} + \{f_{\text{chem}}\}^{\alpha\beta} - \mu\{c\}^{\alpha\beta} - \bar{\boldsymbol{\sigma}} \cdot \{\boldsymbol{\varepsilon}\}^{\alpha\beta} . \tag{36}$$

This work employs a chemo-mechanically fully coupled model in which the elastic energy density depends on the concentration, cf. Eqs. (7), and (25)–(26). This dependence is due in particular to the elastic stiffness, which can be modeled, e.g., by

$$\mathbb{C}^\alpha(c^\alpha) = (1 + \kappa^\alpha(c^\alpha - c_{\text{ref}}^\alpha))\mathbb{C}_{\text{ref}}^\alpha , \tag{37}$$

cf., e.g., [61, Eq. (4)]. Herein, κ^α denotes an isotropic coupling factor and $\mathbb{C}_{\text{ref}}^\alpha$ denotes the stiffness tensor corresponding to the reference concentration c_{ref}^α. The dependence of elastic energy on concentration is also due to the eigenstrains $\tilde{\boldsymbol{\varepsilon}}_{\text{c}}^\alpha$. A common model for these is given by

$$\tilde{\boldsymbol{\varepsilon}}_{\text{c}}^\alpha = (c^\alpha - c_{\text{ref}}^\alpha)\tilde{\boldsymbol{\varepsilon}}_{\text{ref}}^\alpha , \tag{38}$$

cf., e.g., [81, Eq. (1.7)]. Herein, $\tilde{\boldsymbol{\varepsilon}}_{\text{ref}}^\alpha$ denotes a reference strain tensor and c_{ref}^α a reference concentration. According to Vegard's law [82], the lattice parameter of an alloy is a linear function of the concentrations of its constituent elements. Consequently, as the composition of the alloy changes, the lattice parameters change accordingly. Thus, the concentration-dependent eigenstrains are modeled linearly with respect to the concentration.

The evolution of concentration is given using Fick's law of diffusion, cf., e.g., [83, Sect. 5.1], as

$$\dot{c} = -\operatorname{div}(\boldsymbol{j}) . \tag{39}$$

Here, the component flux vector is denoted by $\boldsymbol{j}$ and defined as $\boldsymbol{j} = -\bar{M}\nabla\mu$. The diffusion potential μ is given in Eq. (17). In the multiphase context, the chemical mobility $\bar{M}$ is given by interpolation of the phase-specific chemical mobilities M^α reading

$$\bar{M} = \sum_{\alpha=1}^{N} \phi_\alpha M^\alpha = \sum_{\alpha=1}^{N} \phi_\alpha D^\alpha \left(\frac{\partial \mu^\alpha}{\partial c^\alpha}\right)^{-1} . \tag{40}$$

cf., e.g., [84, Eq. (22)]. The diffusivity within a phase α is denoted by D^α. Accounting for Eq. (16) and (17), the evolution equation of concentration reads

$$\dot{c} = \operatorname{div}\left(\sum_{\alpha=1}^{N}\left(\phi_\alpha D^\alpha \left(\frac{\partial \mu_{\text{chem}}^\alpha}{\partial c^\alpha} + \frac{\partial \mu_{\text{el}}^\alpha}{\partial c^\alpha}\right)^{-1}\right)\nabla\mu\right) . \tag{41}$$

It is significant to note that the component flux is driven by the gradient of a chemo-mechanical diffusion potential. Accordingly, in combination with Eq. (7) it is apparent, that the model is chemo-mechanically fully coupled. It is highlighted, that in contrast to the GCP models [33,59], explicit expressions for c^α in terms of the diffusion potential μ are not required.

2.2. Remarks on the local problem

At each point, the local problem must be solved for the phase-specific concentrations c^α, the jump vectors $\boldsymbol{a}^{\alpha\beta}$ and the diffusion potential μ. The jump conditions are enforced with respect to a single reference phase R. Thus, the number of unknown jump vectors is reduced to $\tilde{N} - 1$, cf., e.g., [45, Sect. 3.2], i.e., $\boldsymbol{a}^{\text{R}\alpha}$ has to be solved with $\text{R} \neq \alpha$. The reader is referred to Appendices A and C for more details on the choice of the reference phase. The resulting system of equations comprises a total of $2\tilde{N}$ equations, reading

$$r_c := \sum_{\alpha=1}^{N} \phi_\alpha c^\alpha - \bar{c} \overset{!}{=} 0 \qquad (1 \text{ equation}) \tag{42}$$

$$\boldsymbol{r}_{\boldsymbol{\sigma}}^{\text{R}\alpha} := \{\boldsymbol{\sigma}\}^{\text{R}\alpha}\boldsymbol{n}^{\text{R}\alpha} \overset{!}{=} \mathbf{0} \quad \forall\, \alpha \in [1, \tilde{N}], \alpha \neq \text{R} \quad (\tilde{N} - 1 \text{ equations}) \tag{43}$$

$$r_\mu^\alpha := \mu_{\text{chem}}^\alpha + \mu_{\text{el}}^\alpha - \mu \overset{!}{=} 0 \quad \forall\, \alpha \in [1, \tilde{N}] \qquad (\tilde{N} \text{ equations}) . \tag{44}$$

The first residual equation, cf. Eq. (42), can be readily derived from the sum condition for the phase-specific concentrations, cf. Eq. (3). The balance of linear momentum on a singular surface serves as the second residual equation in Eq. (43). The third residuum, cf. Eq. (44), represents the equilibrium condition for the chemo-mechanical diffusion potential as introduced in Eq. (17).

The $2\tilde{N}$ unknowns $\{c^\alpha, \boldsymbol{a}^{\text{R}\alpha}, \mu\}$, which are the solution to the system of equations comprising the residuals r_μ^γ, $\boldsymbol{r}_{\boldsymbol{\sigma}}^{\text{R}\gamma}$, and r_c, can be determined through the implementation of a Newton procedure. In this regard, the system

$$\underbrace{\begin{bmatrix} \frac{\partial r_\mu^\gamma}{\partial c^\alpha} & \frac{\partial r_\mu^\gamma}{\partial \boldsymbol{a}^{\text{R}\alpha}} & \frac{\partial r_\mu^\gamma}{\partial \mu} \\ \frac{\partial \boldsymbol{r}_{\boldsymbol{\sigma}}^{\text{R}\gamma}}{\partial c^\alpha} & \frac{\partial \boldsymbol{r}_{\boldsymbol{\sigma}}^{\text{R}\gamma}}{\partial \boldsymbol{a}^{\text{R}\alpha}} & \frac{\partial \boldsymbol{r}_{\boldsymbol{\sigma}}^{\text{R}\gamma}}{\partial \mu} \\ \frac{\partial r_c}{\partial c^\alpha} & \frac{\partial r_c}{\partial \boldsymbol{a}^{\text{R}\alpha}} & \frac{\partial r_c}{\partial \mu} \end{bmatrix}}_{=:\,\underline{\underline{J}}} \underbrace{\begin{bmatrix} \Delta c^\alpha \\ \Delta \boldsymbol{a}^{\text{R}\alpha} \\ \Delta \mu \end{bmatrix}}_{=:\,\underline{\Delta x}} = - \underbrace{\begin{bmatrix} r_\mu^\gamma \\ \boldsymbol{r}_{\boldsymbol{\sigma}}^{\text{R}\gamma} \\ r_c \end{bmatrix}}_{=:\,\underline{R}} \tag{45}$$

must be solved. The matrix in purple constitutes the Jacobian $\underline{\underline{J}}$ and the residuals (green) are written as $\underline{R}$. The unknowns $\underline{\Delta x}$ in blue are solved. A detailed derivation of the system is given in Appendix A. Its implementation is further discussed in Appendix B.

3. Theoretical comparison and analytics

Within this section, a theoretical comparison of different chemo-mechanical coupling approaches is provided. A schematic comparison

Table 2
Comparison of the phase-specific mechanical free energy density, Hooke's law, and the interface assumption for the diffusional potential for the three coupling approaches. In a CMWC model, no concentration-dependent elastic energies are considered, and thus, the mechanical diffusion potential vanishes, i.e., $\mu_{\mathrm{el}}^{\alpha} = 0$. In a CMOC model, concentration-dependent elastic energies are considered within Hooke's law, but although the mechanical diffusion potential does not vanish, i.e., $\mu_{\mathrm{el}}^{\alpha} \neq 0$, it is neglected in the evolution equations. In a CMFC model, concentration-dependent elastic energies are considered, and the diffusion potential comprises a chemical and an elastic contribution.

	Mechanical energy density	Hooke's law	Diffusion potential
CMWC	$f_{\mathrm{el}}^{\alpha} = f_{\mathrm{el}}^{\alpha}(\boldsymbol{\varepsilon}^{\alpha}(\boldsymbol{\phi}, \mathrm{grad}\,(\boldsymbol{u})))$	$\boldsymbol{\sigma}^{\alpha} = \mathbb{C}^{\alpha}[\bar{\boldsymbol{\varepsilon}}^{\alpha} - \bar{\boldsymbol{\varepsilon}}_0^{\alpha}]$	$\mu = \mu_{\mathrm{chem}}^{\alpha}$
CMOC	$f_{\mathrm{el}}^{\alpha} = f_{\mathrm{el}}^{\alpha}(\boldsymbol{\varepsilon}^{\alpha}(\boldsymbol{\phi}, \mathrm{grad}\,(\boldsymbol{u})), c^{\alpha}(\boldsymbol{\phi}, \bar{c}))$	$\boldsymbol{\sigma}^{\alpha} = \mathbb{C}^{\alpha}[\boldsymbol{\varepsilon}^{\alpha} - \bar{\boldsymbol{\varepsilon}}_0^{\alpha} - \bar{\boldsymbol{\varepsilon}}_{\mathrm{c}}^{\alpha}]$	$\mu = \mu_{\mathrm{chem}}^{\alpha}$
CMFC	$f_{\mathrm{el}}^{\alpha} = f_{\mathrm{el}}^{\alpha}(\boldsymbol{\varepsilon}^{\alpha}(\boldsymbol{\phi}, \mathrm{grad}\,(\boldsymbol{u})), c^{\alpha}(\boldsymbol{\phi}, \bar{c}))$	$\boldsymbol{\sigma}^{\alpha} = \mathbb{C}^{\alpha}[\boldsymbol{\varepsilon}^{\alpha} - \bar{\boldsymbol{\varepsilon}}_0^{\alpha} - \bar{\boldsymbol{\varepsilon}}_{\mathrm{c}}^{\alpha}]$	$\mu = \mu_{\mathrm{chem}}^{\alpha} + \mu_{\mathrm{el}}^{\alpha}$

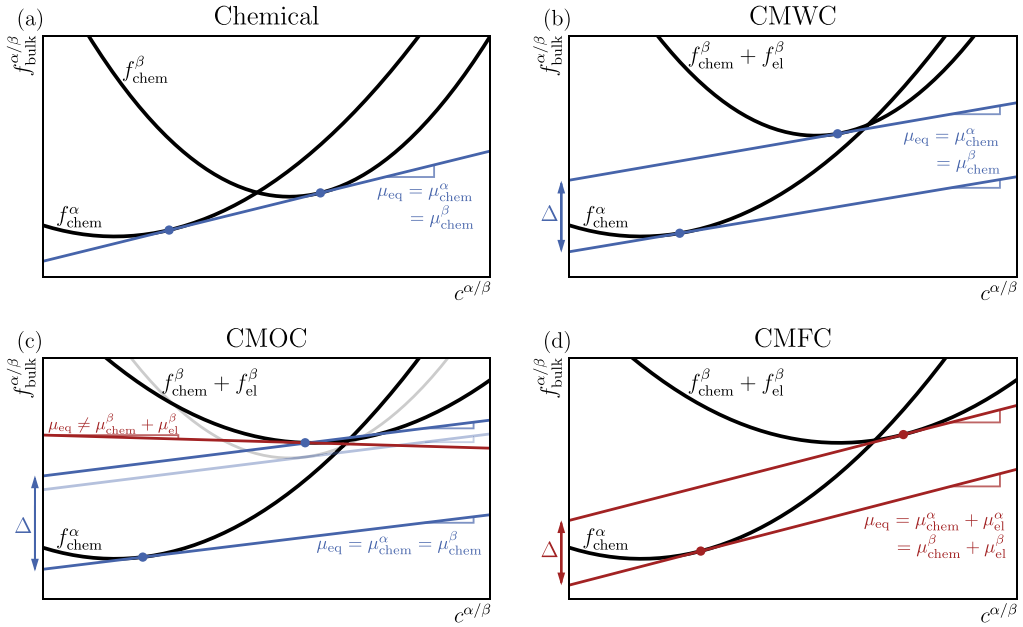

Fig. 1. Schematic depiction of equilibrium conditions for different coupling approaches in terms of the bulk free energy density without curvature contribution. The evaluation of the corresponding tangent construction yields the equilibrium concentrations $c_{\mathrm{eq}}^{\alpha/\beta}$ highlighted with dots. The slope of the tangents corresponds to the diffusion potential in equilibrium μ_{eq}. The distance between two tangents is defined by the rhs Δ in Eq. (46). The equilibrium of a solely chemical system (a) is characterized by a common tangent construction. The CMWC and CMOC models are depicted in (b) and (c), respectively. Here, the chemical diffusion potential constitutes the equilibrium diffusion potential. A CMFC model is represented in (d), where a chemo-mechanical diffusion potential is considered.

is carried out using a two-phase system with one independent component. Furthermore, a comparison scheme based on analytical sharp interface solutions is provided for such a system. Additionally, the scheme can be employed as a benchmark to validate the interaction of chemical, mechanical, and capillary driving forces in chemo-mechanically coupled phase-field methods.

3.1. Coupling approaches in chemo-mechanics

An interfacial equilibrium condition in the SI context is derived from the generalized Gibbs-Thomson equation [85,86]. The equilibrium condition for a chemo-mechanical system without curvature contribution reads

$$\{f_{\mathrm{chem}}\}^{\alpha\beta} - \mu_{\mathrm{eq}}\{c\}^{\alpha\beta} + \{f_{\mathrm{el}}\}^{\alpha\beta} = \bar{\boldsymbol{\sigma}} \cdot \{\boldsymbol{\varepsilon}\}^{\alpha\beta} =: \Delta\,, \tag{46}$$

cf., e.g., [68]. The right-hand side (rhs) is abbreviated as Δ for the following discussion. A comparison of different coupling approaches is made on basis of this equation. The equilibrium diffusion potential μ_{eq}, the elastic energy densities f_{el}^{α}, and, consequently, the stress $\bar{\boldsymbol{\sigma}}$ and strains $\boldsymbol{\varepsilon}^{\alpha}$, are dependent on the coupling approach.

The three coupling approaches – CMWC, CMOC, and CMFC – are distinguished by the diffusion potential μ and the dependencies of the mechanical energy density f_{el}^{α}. If the elastic energy densities f_{el}^{α} depend explicitly on the concentration field $\bar{c}$, the stress field $\bar{\boldsymbol{\sigma}}$, and thus the solution of mechanical equilibrium, cf. Eq. (30), are concentration-dependent. Moreover, the diffusion potential dictates whether mechanical contributions are taken into account in the diffusion equation Eq. (41). Additionally, it impacts the bulk driving force $\Delta_{\mathrm{bulk}}^{\alpha\beta}$ in Eq. (11). For a better understanding, the mechanical energy density, Hooke's law, and the diffusion potential are compared in Table 2. Furthermore, the bulk energy densities f_{bulk} are displayed in Fig. 1 for a solely chemical system (a) and the three coupling approaches (b)–(d), highlighting the equilibrium state through the corresponding tangent construction. Equilibrium concentrations $c_{\mathrm{eq}}^{\alpha/\beta}$ are marked with dots and determined by the points of contact between tangent and free energy densities. Within each scenario, the distance between the tangents equals the rhs Δ in Eq. (46).

- In Fig. 1(a), a solely chemical system is displayed. In this case, the bulk energy densities are given by the chemical free energy densities $f_{\mathrm{chem}}^{\alpha}$ and the elastic energy density vanishes. In equilibrium, the phase concentrations are determined with the well-known common tangent construction, cf., e.g., [87].
- In a CMWC model, the mechanical free energy does not depend on the concentration, i.e., eigenstrains and elastic constants are independent of the concentration, and, as a result, Hooke's law remains unaffected by concentration. In Fig. 1(b), an elastic energy density is present in the phase β. However, it is independent of the concentration, and thus the parabola representing the bulk energy density $f_{\mathrm{bulk}}^{\beta}$ is vertically shifted by a constant offset without a change in its slope. The mechanical diffusion potential $\mu_{\mathrm{el}}^{\beta}$ is zero, and the diffusion potential is given by the chemical diffusion potential, i.e., $\mu = \mu_{\mathrm{chem}}^{\alpha} = \mu_{\mathrm{chem}}^{\beta}$. The equilibrium is characterized by parallel tangents. The distance between the two tangents equals

Table 3
The coefficients used for the parabolic approximation of the chemical free energies are fitted at $T = 970\,\mathrm{K}$ with the Thermo-Calc [88] TCFE7 CALPHAD database.

Coefficient	Unit	Austenite – α	Ferrite – β
A	$\mathrm{J\,mol^{-1}}$	176697.702	7822591.4
B	$\mathrm{J\,mol^{-1}}$	19087.7328	20004.055
C	$\mathrm{J\,mol^{-1}}$	−39957.5051	−40276.6728

the rhs Δ in Eq. (46). Even for the CMWC model, the equilibrium state (e.g., the equilibrium concentration) is shifted due to addition of the elastic energy to the total energy, as predicted by the generalized Gibbs-Thomson equation cf., e.g., [85,86].

- In a CMOC model, a concentration-dependent mechanical energy density is considered, and thus, Hooke's law depends on the concentration. The equilibrium of such a model is visualized in Fig. 1(c) with $f^{\beta}_{\mathrm{el}} = f(c^{\beta})$ and $f^{\alpha}_{\mathrm{el}} = 0$ for illustrative purposes. Consequently, the slope of the total bulk energy density of phase β is impacted and $\mu^{\beta}_{\mathrm{el}} \neq 0$. However, the mechanical diffusion potential is neglected, despite the fact that it is not zero. Hence, $\mu = \mu^{\alpha}_{\mathrm{chem}} = \mu^{\beta}_{\mathrm{chem}}$ is considered. The equilibrium concentrations c^{α} and c^{β} can be determined by the construction of parallel tangents to the chemical energy densities $f^{\alpha}_{\mathrm{chem}}$ and $f^{\beta}_{\mathrm{chem}}$, not to the chemo-mechanical energy density. The rhs Δ in Eq. (46) has to equal the distance between the tangent to $f^{\alpha}_{\mathrm{chem}}$ and the tangent to $f^{\beta}_{\mathrm{chem}}$, which is shifted to intersect with the chemo-mechanical energy density $f^{\beta}_{\mathrm{chem}} + f^{\beta}_{\mathrm{el}}$ exactly at the equilibrium concentration c^{β}. It is clear to see, that the equilibrium diffusion potential μ_{eq}, symbolized by the blue tangents, does not coincide with the chemo-mechanical diffusion potential, symbolized by the tangent to the chemo-mechanical free energy density in red. This discrepancy highlights the inconsistency of considering a concentration-dependent elastic energy density while neglecting the mechanical diffusion potential. In comparison to the previous example, a slight shift in equilibrium concentrations appears. This is due to the concentration-dependency of the stress, which impacts the rhs Δ in Eq. (46), shifting the equilibrium concentrations. It is emphasized that the CMOC model is not consistent with respect to the chemo-mechanical diffusion potential. It is included nevertheless to highlight the impact of coupling approaches.
- In a CMFC model, concentration-dependent eigenstrains (or elastic constants) are considered and coupled into the diffusion equation through a chemo-mechanical diffusion potential. Such a scenario is considered in Fig. 1(d). The equilibrium concentrations c^{α} and c^{β} are determined analogously to the CMWC scenario in Fig. 1(b) by the construction of parallel tangents to the bulk energy density. In this case, the full chemo-mechanical energy density is considered. The slope of the tangents is given by the chemo-mechanical diffusion potential in equilibrium, i.e., $\mu = \mu^{\alpha}_{\mathrm{chem}} + \mu^{\alpha}_{\mathrm{el}} = \mu^{\beta}_{\mathrm{chem}} + \mu^{\beta}_{\mathrm{el}}$. Again, the distance between the parallel tangents equals the rhs Δ in Eq. (46), which depends on the concentration.

3.2. Analytics

With the following SI solution, a scheme is provided to compare the CMFC, CMOC, and CMWC model. This facilitates a comprehensive examination of the impact of chemo-mechanical coupling contributions on equilibrium concentrations and phase fractions when varying the input parameters. In addition to comparing analytical SI solutions for the CMFC, CMOC, and CMWC models, the scheme can be used as a benchmark for validating CMFC model implementations by comparing phase-field simulation (PFS) results with SI solutions. The primary objective of the comparison scheme is to examine the interplay among chemical, capillary, and mechanical driving forces in equilibrium.

The benchmark problems presented in a previous work [68], which employ a two-phase inclusion problem, are utilized and extended. As delineated in the setup III described therein, chemical, mechanical, and capillary driving forces are validated with the use of analytical solutions. The equilibrium conditions, which need to be solved for the equilibrium concentrations c^{α} and c^{β} read

$$
\begin{aligned}
g_1(c^{\alpha}, c^{\beta}) := & \underbrace{\{f_{\mathrm{chem}}\}^{\alpha\beta} - \mu^{\alpha}_{\mathrm{chem}}\{c\}^{\alpha\beta}}_{=:\Delta^{\alpha\beta}_{\mathrm{chem}}} \\
& + \underbrace{\{f_{\mathrm{el}}\}^{\alpha\beta} - \mu^{\alpha}_{\mathrm{el}}\{c\}^{\alpha\beta} - \bar{\boldsymbol{\sigma}} \cdot \{\boldsymbol{\epsilon}\}^{\alpha\beta}}_{=:\Delta^{\alpha\beta}_{\mathrm{mech}}} \\
& + \underbrace{2\bar{\kappa}_S \gamma_{\alpha\beta}}_{=:\Delta^{\alpha\beta}_{\mathrm{cap}}} = 0
\end{aligned}
\tag{47}
$$

$$
g_2(c^{\alpha}, c^{\beta}) := \begin{cases} \mu^{\alpha}_{\mathrm{chem}} + \mu^{\alpha}_{\mathrm{el}} = \mu^{\beta}_{\mathrm{chem}} + \mu^{\beta}_{\mathrm{el}} & \text{(CMFC)} \\ \mu^{\alpha}_{\mathrm{chem}} = \mu^{\beta}_{\mathrm{chem}} \text{ and } \mu^{\alpha}_{\mathrm{el}} = \mu^{\beta}_{\mathrm{el}} = 0 & \text{(CMWC and CMOC)}, \end{cases}
\tag{48}
$$

as reported in [68, Eqs. (46)–(47)]. The averaged stress is calculated as $\bar{\boldsymbol{\sigma}} = (\boldsymbol{\sigma}^{\alpha} + \boldsymbol{\sigma}^{\beta})/2$, as derived in the SI context, cf., e.g., [41]. In addition to the chemical $\Delta^{\alpha\beta}_{\mathrm{chem}}$ and mechanical driving forces $\Delta^{\alpha\beta}_{\mathrm{mech}}$ considered in the theoretical comparison in Eq. (46), a capillary driving force $\Delta^{\alpha\beta}_{\mathrm{cap}}$ is incorporated accounting for curved interfaces. In contrast to the benchmarks for CMWC models outlined in [68], where the equilibrium conditions are formulated in terms of the diffusion potential μ, this work proposes an alternative formulation of the equilibrium equations in Eqs. (47)–(48) in terms of the phase-specific concentrations c^{α}. This approach enables a more flexible exploration of different assumptions regarding the diffusion potential. Using the CMFC model, the second equilibrium condition in Eq. $(48)_1$ corresponds to the equilibrium condition of the diffusional potential described in Eq. (17). Using CMWC or CMOC model, the mechanical diffusion potential $\mu^{\alpha}_{\mathrm{el}}$ is either zero or neglected as elucidated in the previous paragraph, cf. Eq. $(48)_2$.

For evaluation of the scheme, it is necessary to substitute analytical expressions for each driving force. The chemical driving force $\Delta^{\alpha\beta}_{\mathrm{chem}}$ can be, e.g., formulated based on the parabolic approximations of the chemical free energy densities $f^{\alpha}_{\mathrm{chem}}$, as elucidated below. The mechanical $\Delta^{\alpha\beta}_{\mathrm{mech}}$ and capillary driving forces $\Delta^{\alpha\beta}_{\mathrm{cap}}$ are substituted subsequently to defining an appropriate boundary value problem (BVP), as demonstrated in Section 4.2. Subsequently, PFS results can be compared with the SI solution as a benchmark for varying set of parameters. The reader is referred to [68] for a more detailed description of the procedure and to Section 4.2 for the application of the benchmark.

4. Results and discussion

In the following, the presented comparison scheme is employed in order to investigate the impact of the chemo-mechanical coupling approach on equilibrium conditions. Moreover, the CMFC phase-field model is validated. This section also provides illustrative examples to elucidate the impact of the coupling approach on phase transformation kinetics and the diffusion equation. Finally, the presented results are discussed.

4.1. Assumptions

For each phase, the chemical energy density is fitted using a CALPHAD database. For the formulation of the benchmarks and the simulation examples, the Gibbs energies $G^{\alpha}(c^{\alpha})$ with units $\mathrm{J\,mol^{-1}}$ are approximated using parabolic functions and related to the chemical (or Helmholtz) free energy densities $f^{\alpha}_{\mathrm{chem}}$ with units $\mathrm{J\,m^{-3}}$ through the molar Volume V_{m}, i.e.,

$$
f^{\alpha}_{\mathrm{chem}}(c^{\alpha}) = \frac{G^{\alpha}(c^{\alpha})}{V_{\mathrm{m}}} = \frac{1}{V_{\mathrm{m}}}\left(A^{\alpha}(c^{\alpha})^2 + B^{\alpha}c^{\alpha} + C^{\alpha}\right).
\tag{49}
$$

Table 4
Material parameters.

Description	Symbol	Unit	Austenite – α	Ferrite – β	
Young's modulus	E	GPa	146	146	[89]
Poisson's ratio	ν	–	0.33	0.33	[89]
Diffusivity	D	$m^2\,s^{-1}$	3.34×10^{-13}	5.57×10^{-11}	[37]
Molar volume	V_m	$m^3\,mol^{-1}$	7×10^{-6}	7×10^{-6}	[90]
Interfacial energy	$\gamma_{\alpha\beta}$	$J\,m^{-2}$	0.49		[90]
Mobility	$M_{\alpha\beta}$	$m^4\,J^{-1}\,s^{-1}$	1×10^{-11}		this work

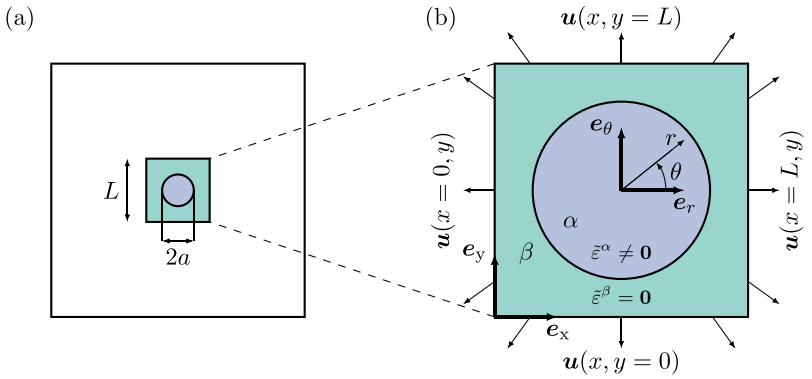

Fig. 2. An inclusion with eigenstrains is embedded within an infinite two-dimensional plate, with both areas exhibiting identical elastic properties (a). A finite section of that plate is considered, analogously to [68, Fig. 3] as simulation domain (b). Dirichlet boundary conditions are applied to the boundary of the finite section according to analytical solutions, cf., e.g., [93,94]. The analytical solutions are given in Appendix D with respect to the polar coordinate system at the center of the domain.

Herein, Eq. (18) is considered. An example workflow to fit the coefficients A^α, B^α, and C^α with units $J\,mol^{-1}$ from a CALPHAD database is given, e.g., in [91]. Furthermore, alternative approximation functions are reported therein.

With Eq. (49) the chemical diffusion potential is derived as

$$\mu^\alpha_{\text{chem}} = \frac{\partial f^\alpha_{\text{chem}}}{\partial c^\alpha} = \frac{2A^\alpha c^\alpha + B^\alpha}{V_m}\,. \tag{50}$$

In the following examples, the stiffnesses $\mathbb{C}^\alpha$ are considered constant and the dependence of the elastic energy densities on the concentration is realized through concentration-dependent eigenstrains as defined in Eq. (38). With Eqs. $(16)_2$, (26), and (38), the mechanical diffusion potential reads

$$\mu^\alpha_{\text{el}} = \frac{\partial f^\alpha_{\text{el}}}{\partial c^\alpha} = -\tilde{\boldsymbol{\varepsilon}}^\alpha_{\text{ref}} \cdot \boldsymbol{\sigma}^\alpha\,. \tag{51}$$

The following calculations and simulations are based on an Fe-C alloy, wherein an austenitic phase α and a ferritic phase β are taken into consideration. The coefficients of the parabolic chemical free energy approximation, cf. Eq. (49), are fitted with the use of the TCFE7 CALPHAD database in the Thermo-Calc Software [88] for a temperature $T = 970\,K$. As input for a least square method, the Gibbs energy of each phase is computed separately in the vicinity of the respective equilibrium concentrations $c^\alpha_{\text{eq}} = 4.4382$ at.-% and $c^\beta_{\text{eq}} = 0.101655$ at.-%. The fitted coefficients are summarized in Table 3. Any additional material parameter used for the simulation is reported in Table 4. All phase-field simulations, including the chemo-mechanical coupling, were performed using the Pace3D in-house simulation software [92].

4.2. Comparison scheme and benchmark

4.2.1. Objective and description

In this first example, the SI solution presented in Section 3.2 is employed. The results are evaluated to compare the impact of coupling approaches on equilibrium phase-fractions and concentrations. Additionally, the model derived in Section 2 is validated.

In the initial step, a BVP is defined in order to substitute the driving forces in Eqs. (47)–(48). To derive the mechanical driving force $\Delta^{\alpha\beta}_{\text{mech}}$ for the equilibrium conditions, an inclusion problem based on Eshelby's inclusion problem [95–97] is employed. The analytical solution to the mechanical BVP is adopted from [93, Eqs. (16)–(17)]. They are reported in Appendix D for the sake completeness. In [94] equivalent formulations in terms of Airy stress functions can be found. Analogously to the approach presented in [68], a finite section of the infinite plate for which the solution is formulated is used. The boundary conditions are visualized in Fig. 2. The eigenstrain within the inclusion is modeled with a constant isotropic contribution independent of the concentration $\tilde{\varepsilon}^\alpha_0$ and an isotropic but concentration-dependent contribution $\tilde{\varepsilon}^\alpha_c$, i.e.,

$$\tilde{\varepsilon}^\alpha_0 = \tilde{\varepsilon}^\alpha_0 \boldsymbol{I} \quad \text{and} \quad \tilde{\varepsilon}^\alpha_c = (c^\alpha - c^\alpha_{\text{ref}})\tilde{\varepsilon}^\alpha_{\text{ref}} \boldsymbol{I}\,. \tag{52}$$

Herein, $\boldsymbol{I}$ denotes the second-order identity tensor. The chemical equilibrium concentration is taken as reference, i.e., $c^\alpha_{\text{ref}} = 4.4382$ at.-%. Within the surrounding matrix the eigenstrains are zero, i.e., $\tilde{\boldsymbol{\varepsilon}}^\beta(c^\beta) = \mathbf{0}$ is considered and, thus, $\mu^\beta_{\text{el}} = 0$. The derivation of the mechanical driving force is given in Appendix E in more detail. The derivation of the capillary driving force $\Delta^{\alpha\beta}_{\text{cap}}$, which is based on geometrical considerations and the lever rule, is given in more detail in [68]. The curvature κ_S of the circular inclusion is given in [68, Eqs. (41)–(42)]. The chemical driving force is derived by substituting Eq. (49). The final equilibrium conditions for all three coupling approaches are reported in Appendix E. The equilibrium conditions, cf. Eq. (E.7)–(E.12), are solved for the concentrations $c^\alpha_{\text{eq}}, c^\beta_{\text{eq}}$ in equilibrium. For the following comparison with PFS results, the equilibrium phase fraction ξ^α_{eq} is computed by substituting the concentrations obtained by SI solutions into the lever rule

$$\xi^\alpha_{\text{eq}} = \frac{|c_{\text{tot}} - c^\beta_{\text{eq}}|}{|c^\alpha_{\text{eq}} - c^\beta_{\text{eq}}|}\,, \tag{53}$$

cf., e.g., [98]. The average carbon content c_{tot} remains constant throughout the simulation by enforcing zero concentration flux on all boundaries.

4.2.2. Results

A study is conducted by separately increasing the total carbon concentration c_{tot}, the interfacial energy $\gamma_{\alpha\beta}$, the reference eigenstrain $\tilde{\varepsilon}^\alpha_{\text{ref}}$,

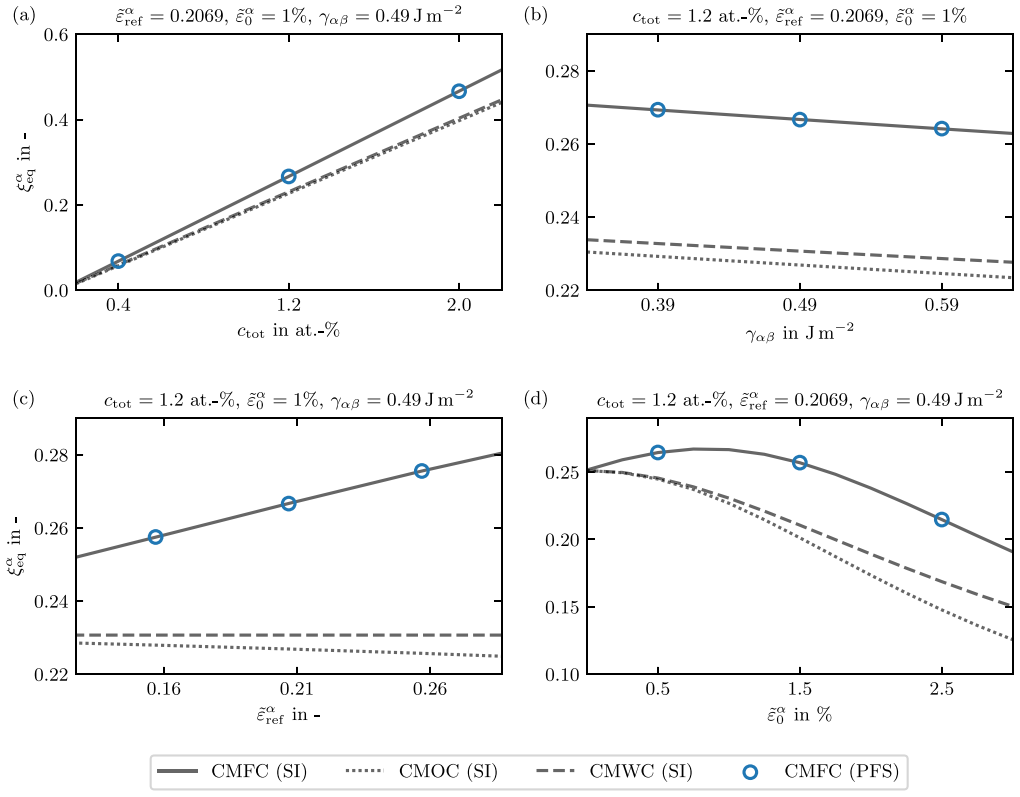

Fig. 3. The equilibrium phase fractions $\xi^{\alpha}_{\mathrm{eq}}$ of the inclusion are compared for the three coupling approaches with variation of the total concentration c_{tot} (a), the interfacial energy $\gamma_{\alpha\beta}$ (b), the reference strain factor $\tilde{\varepsilon}^{\alpha}_{\mathrm{ref}}$ for concentration-dependent eigenstrains (c), and the concentration-independent eigenstrain ε^{α}_{0} (d). The derived SI solutions using the CMFC, CMOC, and CMWC model are represented by solid, dotted, and dashed lines, respectively. PFS results obtained with CMFC model are represented by circular marks.

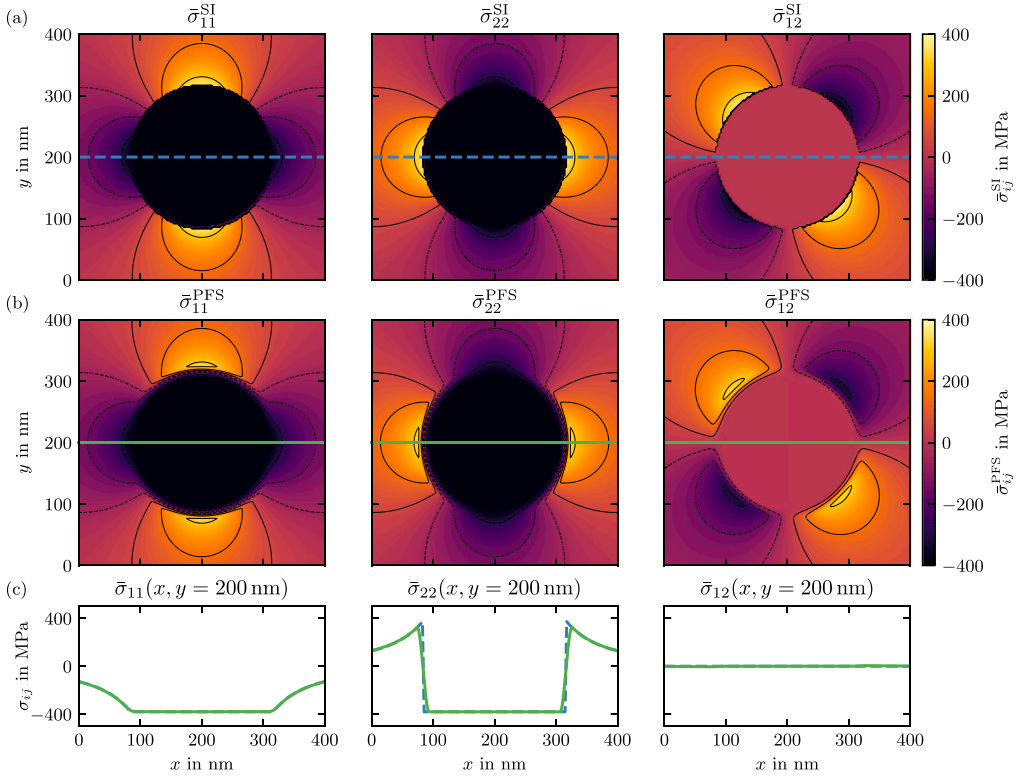

Fig. 4. Comparison of stress fields $\bar{\sigma}_{11}$, $\bar{\sigma}_{22}$, and $\bar{\sigma}_{12}$ for $c_{\mathrm{tot}} = 1.2$ at.-%, $\tilde{\varepsilon}^{\alpha}_{0} = 0.5\%$, $\tilde{\varepsilon}^{\alpha}_{\mathrm{ref}} = 0.2069$, and $\gamma_{\alpha\beta} = 0.49\,\mathrm{J\,m^{-2}}$. The SI solutions are visualized in (a) and the PFS results in (b) as indicated by the superscripts. Contour lines are set to fixed values for each stress component. Both results are compared in (c) along a horizontal line indicated in each plot. Apart from the diffuse interface region, the solutions align.

and the concentration-independent eigenstrain contribution $\tilde{\varepsilon}_0^\alpha$. The results are visualized in Fig. 3. The SI solutions are depicted using solid, dotted, and dashed lines in gray for the CMFC, CMOC, and CMWC model, respectively. PFS are conducted until equilibrium is reached. The phase fraction of PFS results is calculated with $\xi^\alpha = \int_\mathcal{V} \phi_\alpha \, \mathrm{d}v / (\int_\mathcal{V} \mathrm{d}v)$. Each PFS result is marked with a circular mark. Two primary observations can be derived from this study. Firstly, a comparison of the analytically derived SI solutions can be used to assess the differences between the various coupling theories. Secondly, this scheme is used as a benchmark to validate the proposed CMFC phase-field model. Regarding the first observation, the analytically derived SI solutions are compared. A significant influence of the applied coupling on the analytical solution is observed. As visible in Fig. 3(a), when increasing the average carbon concentration c_{tot} the equilibrium size of the austenitic inclusion α increases. Additionally, the discrepancy between the CMFC, CMOC, and CMWC results increases, as the impact of concentration-dependent driving forces increases. In Fig. 3(b), the effect of increased interfacial energy $\gamma_{\alpha\beta}$ is visualized. With increased $\gamma_{\alpha\beta}$ the equilibrium size of the inclusion decreases. Since $\gamma_{\alpha\beta}$ is not coupled to the concentration in any way, the offset of the results predicted by CMFC model to the results predicted by CMWC and CMOC model is constant. In Fig. 3(c), the reference eigenstrain $\tilde{\varepsilon}_{\mathrm{ref}}^\alpha$ is varied. With increasing $\tilde{\varepsilon}_{\mathrm{ref}}^\alpha$, the inclusion size increases for the CMFC model. Since no concentration-dependent eigenstrain is considered in the CMWC model, there is no impact and the predicted equilibrium phase fraction of the inclusion is fixed. Interestingly, when evaluating the CMOC approach, the inclusion size decreases with increasing $\tilde{\varepsilon}_{\mathrm{ref}}^\alpha$. In this case, the mechanical diffusion potential μ_{el} is neglected, while the stress depends on the concentration. In Fig. 3(d), the constant concentration-independent eigenstrain is varied. Again, the difference between CMFC, CMOC, and CMWC is clearly visible. An increase in $\tilde{\varepsilon}_0^\alpha$ leads to a nonlinear decrease in the inclusion phase-fraction employing a CMWC or CMOC model. With the CMFC model, first an increase is observed followed by a decrease as soon as the concentration-independent eigenstrain becomes more dominant. It has to be emphasized, that a change in the mechanical driving force, has an impact on CMFC results as well as on CMOC and CMWC results. In regard to the second observation, the PFS results obtained using a CMFC model are validated against SI solutions. A very good agreement of the PFS results and the SI solution is clearly visible in all four studies. Furthermore, the analytically derived stress fields are compared with the ones obtained with PFS to facilitate additional validation. In Fig. 4, the stress fields $\bar{\sigma}_{11}$, $\bar{\sigma}_{22}$, and $\bar{\sigma}_{12}$ are visualized. The SI solution (Fig. 4(a)) is compared with the PFS results (Fig. 4(b)) for $c_{\mathrm{tot}} = 1.2$ at.-%, $\tilde{\varepsilon}_0^\alpha = 0.5\,\%$, $\tilde{\varepsilon}_{\mathrm{ref}}^\alpha = 0.2069$, and $\gamma_{\alpha\beta} = 0.49\,\mathrm{J\,m^{-2}}$. Convincing agreement of the stress fields obtained by PFS and SI considerations is achieved. Apart from the diffuse interface region, the solutions align, cf. Fig. 4(c).

4.3. Kinetic example

4.3.1. Objective and description

The following example is provided to elucidate the impact of the chemo-mechanical coupling approach on transformation kinetics. In this regard, a quasi one-dimensional domain is created with two phases austenite α and ferrite β, cf. Fig. 5(a). Initially, the austenite phase fraction ξ^α is 2% and the carbon content c^α is set to the equilibrium concentration. The carbon concentration in ferrite c^β is adjusted such that the average carbon content c_{tot} is 3.0 at.-%. Zero-flux boundary conditions are employed for the concentration field. The diffusivities D^α are obtained from DICTRA and the mobility $M_{\alpha\beta}$ is calibrated by comparing the solely chemical simulation (CHEM) to DICTRA results. A timestep of $\Delta t = 10\,\mathrm{ns}$ is chosen. The left and right boundaries are subjected to a stress boundary condition with $\boldsymbol{\sigma} = \sigma_0 \boldsymbol{e}_{\mathrm{x}} \otimes \boldsymbol{e}_{\mathrm{x}}$ and $\sigma_0 = 100\,\mathrm{MPa}$. The displacement is fixed in the y-direction. In the CMOC and CMFC simulations, concentration-dependent eigenstrains with $\tilde{\boldsymbol{\varepsilon}}_{\mathrm{ref}}^\alpha = 0.2096\boldsymbol{I}$ and $c_{\mathrm{ref}}^\alpha = 0$, and $\tilde{\boldsymbol{\varepsilon}}_{\mathrm{ref}}^\beta = \boldsymbol{0}$ are considered, cf. Eq. (38).

4.3.2. Results

In Fig. 5(b), the evolution of the austenite phase fraction ξ^α is depicted for the chemical simulation (CHEM), all coupling approaches (CMWC, CMOC, CMFC), and the DICTRA simulation. CHEM and CMWC exhibit equivalent transformation kinetics. In comparison with the other coupling approaches, in a CMFC simulation, the austenite reaches its equilibrium phase fraction faster. Moreover, the equilibrium phase fraction is higher. Conversely, a CMOC simulation predicts a reduced growth rate and a smaller equilibrium phase fraction. For reasons of clarity, only the carbon profiles along the x-axis obtained by the CMWC and CMFC approaches are compared in Fig. 5(c). In this example, the carbon profile obtained with a CMWC approach is equivalent to the solely chemical case CHEM. This comparison also shows that a CMFC model leads to faster growth of the austenitic phase. As demonstrated in this example, the transformation kinetics are impacted by the chemo-mechanical coupling approach.

4.4. Diffusion example

4.4.1. Objective and description

Within this third example, no phase-evolution is investigated. Instead, a diffusion problem is considered in two (2D) and three dimensions (3D) to highlight the different interplay of component fluxes and stresses for different coupling approaches.

A domain with multiple austenitic grains is considered. These grains are identical except for their orientation. Each grain is subject to a random rotation described by a rotation tensor $\boldsymbol{Q}^\alpha$. With the CMOC and CMFC model, a concentration-dependent eigenstrain $\tilde{\boldsymbol{\varepsilon}}_{\mathrm{c}}^\alpha = \boldsymbol{Q}^\alpha \star \left(\tilde{\boldsymbol{\varepsilon}}_{\mathrm{ref}}(c^\alpha - c_{\mathrm{ref}})\right)$ is considered with an anisotropic reference strain $\tilde{\boldsymbol{\varepsilon}}_{\mathrm{ref}} = 0.1\left(\boldsymbol{e}_{\mathrm{x}} \otimes \boldsymbol{e}_{\mathrm{x}} + 1/2\boldsymbol{e}_{\mathrm{y}} \otimes \boldsymbol{e}_{\mathrm{y}}\right)$ and $c_{\mathrm{ref}} = 0$ in 2D and $\tilde{\boldsymbol{\varepsilon}}_{\mathrm{ref}} = 0.2069(\boldsymbol{e}_{\mathrm{x}} \otimes \boldsymbol{e}_{\mathrm{x}} + 2/3\boldsymbol{e}_{\mathrm{y}} \otimes \boldsymbol{e}_{\mathrm{y}} + 1/3\boldsymbol{e}_{\mathrm{z}} \otimes \boldsymbol{e}_{\mathrm{z}})$ and $c_{\mathrm{ref}} = 2.44$ at.-% in 3D. The coordinate origin is in the bottom (front) left corner of the domain in 2D (and 3D). The rotation is described using the Rayleigh product, cf., e.g., [99, Sect. 1.2.4]. For the 2D simulation, the initial concentration field $\bar{c}$ is artificially created with an area of elevated carbon concentration and an area with comparatively lower concentration of carbon, cf. Fig. 6 (first row). For the 3D simulation, the initial concentration field is homogeneous, i.e., $\bar{c}(\boldsymbol{x}, t = 0) = c_{\mathrm{tot}}$. As a result of the chosen boundary conditions for the component flux $\boldsymbol{j}$, the average carbon content in domain is constant throughout all following simulations in 2D and 3D, i.e., $c_{\mathrm{tot}} \equiv 3.44$ at.-%. In the 2D case, the component flux $\boldsymbol{j}$ is considered periodic on the top and bottom boundary, as is the displacement $\boldsymbol{u}$. On the left and right boundary the component flux $\boldsymbol{j}$ is set to zero and a zero stress vector is assumed. In the 3D case, periodic boundary conditions are enforced on all boundaries for the component flux $\boldsymbol{j}$ and the displacement field $\boldsymbol{u}$.

4.4.2. Results

In Fig. 6, the results of the study in 2D are presented at times $t_0 < t_1 < t_2$. At time t_2 the system is in equilibrium. Employing the CMWC, cf. Fig. 6(a), and the CMOC model, cf. Fig. 6(b), the carbon diffuses equally resulting in a homogeneous distribution of carbon in equilibrium. In the CMWC case, the stresses are independent of the concentration, thus the stress is zero in the entire domain $\bar{\sigma}_{\mathrm{vM}} \equiv 0$. The CMOC model, takes concentration-dependent eigenstrains into consideration, thus a heterogeneous stress field is observed. Using the CMFC model Fig. 6(c), the diffusion fluxes of carbon are heterogeneous resulting in a heterogeneously distributed carbon in equilibrium. The predicted stress field is heterogeneous as well. In Fig. 7, the results of the study in 3D are displayed. The CMWC model Fig. 7(a) does not consider concentration-dependent eigenstrains and no diffusion flux is induced. Thus, in equilibrium a homogeneous concentration field $\bar{c}$ is observed accompanied by the absence of stresses. The CMOC model Fig. 7(b), which incorporates concentration-dependent eigenstrains but no coupling contributions in the diffusion equation, results in an inhomogeneous stress distribution that does not lead to diffusion fluxes. The

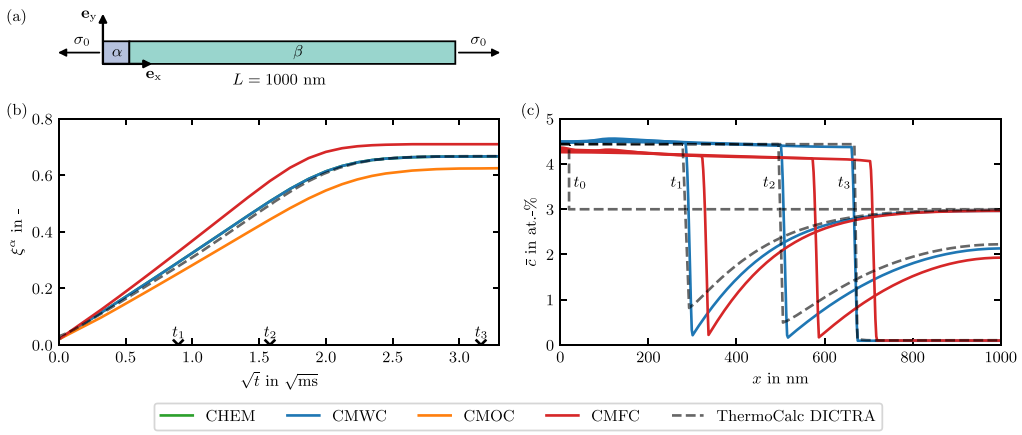

Fig. 5. Comparison of transformation kinetics. A domain with an initially small region of austenite α and a large region of ferrite β is subjected to a boundary stress $\boldsymbol{\sigma} = \sigma_0 \boldsymbol{e}_x \otimes \boldsymbol{e}_x$ (a). The austenite region is initialized with its equilibrium carbon content, while the ferrite region is initialized so that the average carbon content in the entire domain is $c_{tot} = 3.0$ at.-%. The chemical simulation without mechanical loading (CHEM) is calibrated with DICTRA. The $\alpha\beta$-interface moves to the right and approaches the equilibrium phase fraction ξ^α (b). The carbon profiles obtained from a solely chemical simulation matches the DICTRA prediction well (c). In both (b) and (c), the impact of the chemo-mechanical coupling approach is clearly visible.

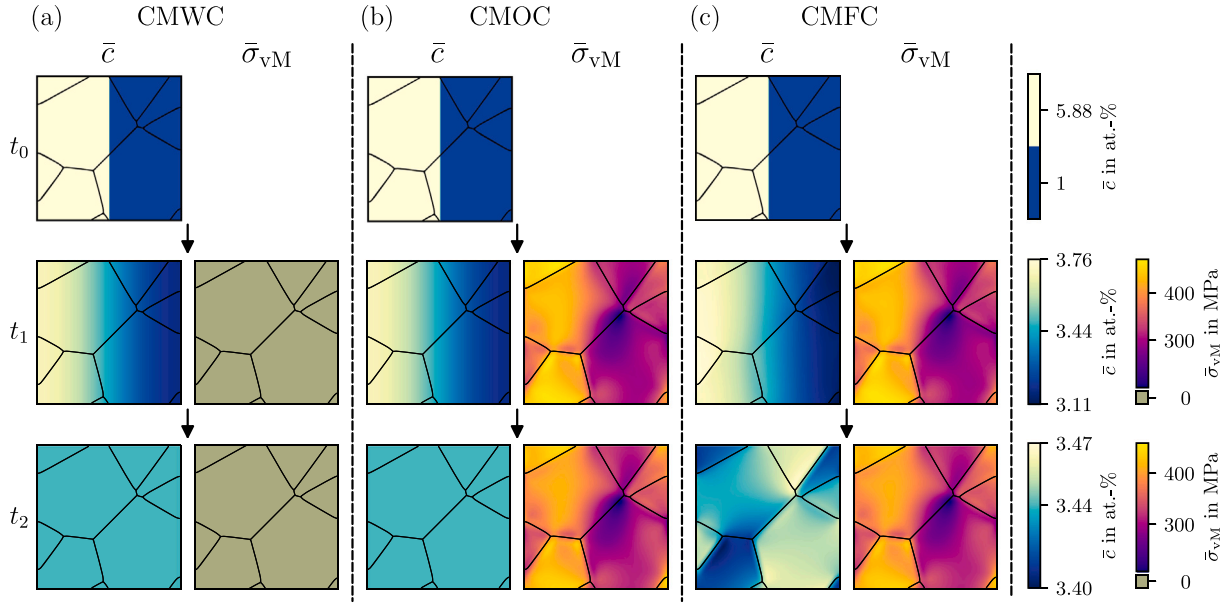

Fig. 6. Diffusion example in 2D. A concentration field $\bar{c}$ is created featuring a carbon-rich and a carbon-depleted area (first row). This artificially constructed field is then utilized as an input for a detailed analysis of the diffusion behavior predicted by the three coupling approaches. According to the CMWC model (a), diffusion fluxes are homogeneous, and carbon diffuses evenly. This results in an equilibrium state in which a homogeneous distribution of carbon is observed. Since no concentration-dependent eigenstrains are considered, the von Mises stress $\bar{\sigma}_{\text{vM}}$ vanishes. Similarly, according to the CMOC model (b), the carbon diffuses evenly. Additionally, concentration-dependent eigenstrains are considered, resulting in a heterogeneous von Mises stress field $\bar{\sigma}_{\text{vM}}$. Utilizing the CMFC model (c), diffusion fluxes are heterogeneous and the carbon does not diffuse evenly. In equilibrium, the carbon is distributed heterogeneously which is due to the heterogeneous stress field $\bar{\sigma}_{\text{vM}}$.

CMFC model Fig. 7(c) considers concentration-dependent eigenstrains and incorporates coupling contributions into the diffusion equation. In addition to the inhomogeneous stress distribution, diffusion fluxes are induced and the initially homogeneous carbon distribution becomes inhomogeneous in equilibrium. For a discussion of numerical aspects, the reader is referred to Appendix F.

4.5. Discussion

The proposed benchmark allows the validation of the implementation of a chemo-mechanically fully coupled phase-field model by validating the interplay of chemical, capillary, and mechanical driving forces. Moreover, it is demonstrated with the use of analytical SI solutions that the selected coupling approach has a strong impact on equilibrium concentrations and phase-fractions. It is important to note, that a one-sided coupling described in the CMOC model can result in stronger deviations from the CMFC results compared to those observed with the CMWC model. In some cases, an opposing behavior of CMOC and CMFC model is revealed. This observation can be attributed to the neglect of coupling contributions in the CMOC model. As predicted by the generalized Gibbs-Thomson equation, it is highlighted, that the incorporation of mechanical driving forces yields a shift in equilibrium compositions regardless of the selected coupling approach.

Furthermore, it is demonstrated, that the chemo-mechanical coupling approach impacts phase transformation kinetics. Different growth rates are observed for the different coupling approaches.

As shown in the case of 2D and 3D diffusion examples, only with a CMFC model it is possible to account for stress-driven diffusion and diffusion-induced stresses. This is due to the component fluxes which depend on the gradient of the chemo-mechanical diffusion potential,

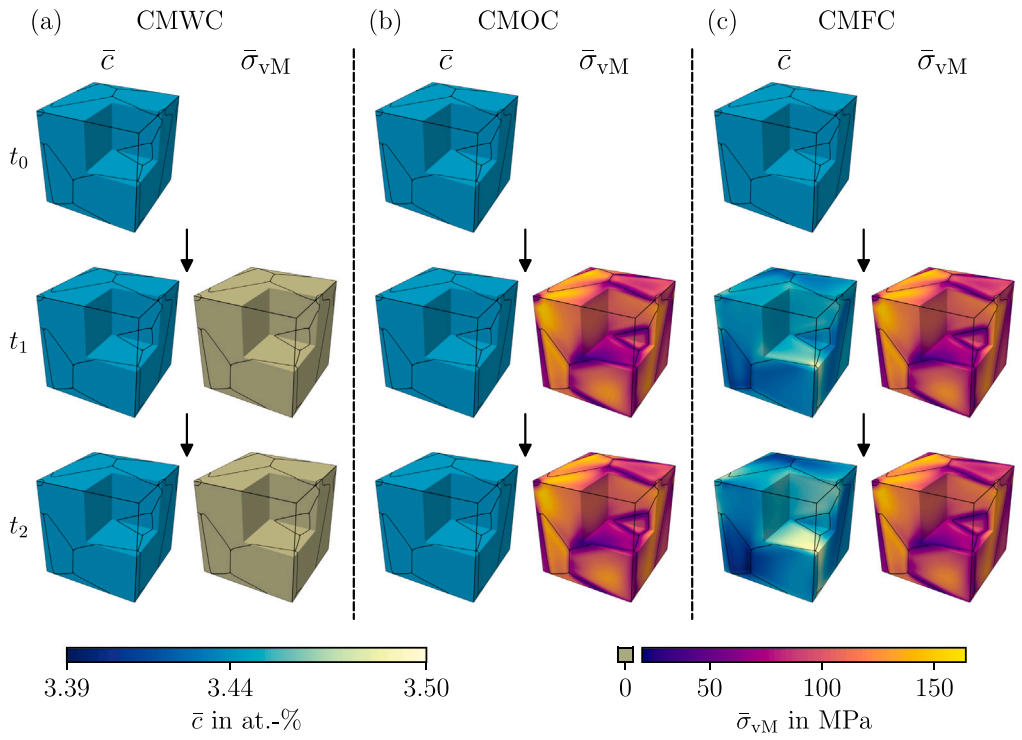

Fig. 7. Diffusion example in 3D. The initial carbon distribution is homogeneous (first row). With the CMWC model (a) no diffusion flux is induced and a zero von Mises stress $\bar{\sigma}_{\mathrm{vM}}$ is predicted. The same initial configuration, employing the CMOC model (b), yields an inhomogeneous stress distribution $\bar{\sigma}_{\mathrm{vM}}$ that does not induce diffusion fluxes. The CMFC model (c) predicts both an inhomogeneous stress field $\bar{\sigma}_{\mathrm{vM}}$ and a non-zero carbon flux, such that the initially homogeneous carbon distribution becomes inhomogeneous.

which depends on the stress, cf. Eqs. (41) and (51). One may choose a CMOC model for the purpose of chemo-mechanical simulations, if the calculation of composition-dependent stresses are of primary interest. However, it is imperative to acknowledge, that the resulting equilibrium concentrations are inconsistent with the chemo-mechanical diffusion potential. Notwithstanding its potential limitations, the CMOC approach is included herein for illustrative purposes.

5. Conclusion

In summary, the central objectives of the work at hand are, first, to derive a chemo-mechanically fully coupled multiphase-field model; second, to provide a scheme that facilitates comparison of coupling approaches and validation of phase-field methods; and third, to examine the impact of the selected chemo-mechanical coupling approach in multiphase-field methods on the evolution of microstructures, the final equilibrium state, and the component diffusion. In this regard, the following conclusions are derived:

The proposed chemo-mechanically fully coupled multiphase-field model accounts for balance equations on singular surfaces and Hadamard jump conditions in the diffuse interface region. As a consequence, analytical sharp interface solutions are reproduced. The model formulation allows to account for the dependence of mechanical energy densities on the composition in terms of concentration-dependent eigenstrains or elastic constants. The simulation results presented in this work assume a constant stiffness tensor and account for concentration-dependent eigenstrains.

The proposed comparison scheme facilitates the evaluation and comparison of different chemo-mechanical coupling approaches based on analytical sharp interface solutions. Furthermore, it can be employed as a benchmark, to validate chemo-mechanically coupled phase-field methods. In this regard, phase-field simulation results are compared with analytical sharp interface solutions. The simplicity of the formulation enables straightforward modifications such as different boundary value problems.

The following key findings have emerged from the present investigation: The chemo-mechanical coupling approach has a strong influence on the evolution of microstructures, phase transformation kinetics, the final equilibrium state, and the component diffusion. A chemo-mechanically weakly coupled phase-field model (CMWC) is not appropriate to account for stress-driven component fluxes or diffusion-induced stresses. However, a weak coupling through the bulk driving forces results in a shift in equilibrium concentration as predicted by the generalized Gibbs-Thomson equation. The utilization of a chemo-mechanically one-sided coupled phase-field model (CMOC) facilitates the computation of diffusion-induced stresses. However, its formulation is inconsistent with the chemo-mechanical diffusion potential since the mechanical diffusion potential is neglected. In order to account for concentration-dependent mechanical energy densities, and thus diffusion-induced stresses, as well as stress-driven diffusion, it is necessary to employ a chemo-mechanically fully coupled phase-field model (CMFC). Only with the CMFC model chemo-mechanical coupling contributions are accounted for in the diffusion equation and during stress calculation.

CRediT authorship contribution statement

Thea Kannenberg: Visualization, Software, Investigation, Conceptualization, Writing – original draft, Validation, Methodology, Formal analysis. **Andreas Prahs:** Supervision, Writing – review & editing. **Bob Svendsen:** Writing – review & editing. **Britta Nestler:** Supervision, Writing – review & editing, Funding acquisition. **Daniel Schneider:** Writing – review & editing, Project administration, Conceptualization, Supervision, Methodology.

Declaration of competing interest

The authors declare that they have no known competing financial interests or personal relationships that could have appeared to influence the work reported in this paper.

$$\begin{bmatrix} \tilde{N}\times\tilde{N} & \tilde{N}\times(\tilde{N}-1)D & \tilde{N}\times 1 \\ (\tilde{N}-1)D\times\tilde{N} & (\tilde{N}-1)D\times(\tilde{N}-1)D & (\tilde{N}-1)D\times 1 \\ 1\times\tilde{N} & 1\times(\tilde{N}-1)D & 1\times 1 \end{bmatrix} \begin{bmatrix} \tilde{N}\times 1 \\ (\tilde{N}-1)D\times 1 \\ 1\times 1 \end{bmatrix} = \begin{bmatrix} \tilde{N}\times 1 \\ (\tilde{N}-1)D\times 1 \\ 1\times 1 \end{bmatrix}. \tag{A.1}$$

Box I.

Acknowledgments

TK gratefully acknowledges the financial support of the German Research Foundation (DFG) within the project "Giga-NANOBAIN" (Proj. No. 490856143). AP gratefully acknowledges the financial support by the Federal Ministry of Education and Research (BMBF), Germany within the joint Project "05M2022 - DASEA-4-SOFC". DS and BN are thankful for funding research on chemo-mechanical modeling developments through the Helmholtz association, within program "Materials Systems Engineering (MSE)" (Proj. No. 43.31.01).

Appendix A. Detailed derivation of the local problem

In this section, the local problem, cf. Eq. (45), is derived in detail. Furthermore, remarks on the system size are provided to support implementation.

The Jacobian defined in Eq. (45) is of size $(\tilde{N}+(\tilde{N}-1)D+1)\times(\tilde{N}+(\tilde{N}-1)D+1)$, with dimension D. The size of the equation system and its constituents is given in Box I. Within each grid point, the phases are rearranged according to their phase fraction, in descending order. In this manner, the phase with the largest phase fraction, phase 1, is selected as reference phase. A more detailed discussion on the reference phase is given in Appendix C. In detail, the system of equations defining the local problem reads

$$\begin{bmatrix} \frac{\partial r_\mu^1}{\partial c^1} & \cdots & \frac{\partial r_\mu^1}{\partial c^{\tilde{N}}} & \frac{\partial r_\mu^1}{\partial \boldsymbol{a}^{12}} & \cdots & \frac{\partial r_\mu^1}{\partial \boldsymbol{a}^{1\tilde{N}}} & \frac{\partial r_\mu^1}{\partial \mu} \\ \vdots & \ddots & \vdots & \vdots & \ddots & \vdots & \vdots \\ \frac{\partial r_\mu^{\tilde{N}}}{\partial c^1} & \cdots & \frac{\partial r_\mu^{\tilde{N}}}{\partial c^{\tilde{N}}} & \frac{\partial r_\mu^{\tilde{N}}}{\partial \boldsymbol{a}^{12}} & \cdots & \frac{\partial r_\mu^{\tilde{N}}}{\partial \boldsymbol{a}^{1\tilde{N}}} & \frac{\partial r_\mu^{\tilde{N}}}{\partial \mu} \\ \frac{\partial \boldsymbol{r}_\sigma^{12}}{\partial c^1} & \cdots & \frac{\partial \boldsymbol{r}_\sigma^{12}}{\partial c^{\tilde{N}}} & \frac{\partial \boldsymbol{r}_\sigma^{12}}{\partial \boldsymbol{a}^{12}} & \cdots & \frac{\partial \boldsymbol{r}_\sigma^{12}}{\partial \boldsymbol{a}^{1\tilde{N}}} & \frac{\partial \boldsymbol{r}_\sigma^{12}}{\partial \mu} \\ \vdots & \ddots & \vdots & \vdots & \ddots & \vdots & \vdots \\ \frac{\partial \boldsymbol{r}_\sigma^{1\tilde{N}}}{\partial c^1} & \cdots & \frac{\partial \boldsymbol{r}_\sigma^{1\tilde{N}}}{\partial c^{\tilde{N}}} & \frac{\partial \boldsymbol{r}_\sigma^{1\tilde{N}}}{\partial \boldsymbol{a}^{12}} & \cdots & \frac{\partial \boldsymbol{r}_\sigma^{1\tilde{N}}}{\partial \boldsymbol{a}^{1\tilde{N}}} & \frac{\partial \boldsymbol{r}_\sigma^{1\tilde{N}}}{\partial \mu} \\ \frac{\partial r_c}{\partial c^1} & \cdots & \frac{\partial r_c}{\partial c^{\tilde{N}}} & \frac{\partial r_c}{\partial \boldsymbol{a}^{12}} & \cdots & \frac{\partial r_c}{\partial \boldsymbol{a}^{1\tilde{N}}} & \frac{\partial r_c}{\partial \mu} \end{bmatrix} \begin{bmatrix} \Delta c^1 \\ \vdots \\ \Delta c^{\tilde{N}} \\ \Delta \boldsymbol{a}^{12} \\ \vdots \\ \Delta \boldsymbol{a}^{1\tilde{N}} \\ \Delta \mu \end{bmatrix} = - \begin{bmatrix} r_\mu^1 \\ \vdots \\ r_\mu^{\tilde{N}} \\ \boldsymbol{r}_\sigma^{12} \\ \vdots \\ \boldsymbol{r}_\sigma^{1\tilde{N}} \\ r_c \end{bmatrix}. \tag{A.2}$$

In the following derivations, the assumptions presented in Section 4.1 are employed, i.e., in particular Eqs. (49)–(51) are considered. After some rearrangement and substitution of the strains, strain jumps, and consideration of the symmetries of the stiffness tensor and of the stress, i.e., $\mathbb{C}^\alpha = (\mathbb{C}^\alpha)^{\mathsf{T}_\mathrm{H}} = (\mathbb{C}^\alpha)^{\mathsf{T}_\mathrm{L}} = (\mathbb{C}^\alpha)^{\mathsf{T}_\mathrm{R}}$ and $\boldsymbol{\sigma}^\alpha = (\boldsymbol{\sigma}^\alpha)^{\mathsf{T}}$, the second residual in Eq. (43) is reformulated as

$$\begin{aligned} \boldsymbol{r}_\sigma^{1\alpha} &= \left(\frac{\partial f_\mathrm{el}^1}{\partial \boldsymbol{\varepsilon}^1} - \frac{\partial f_\mathrm{el}^\alpha}{\partial \boldsymbol{\varepsilon}^\alpha}\right)\boldsymbol{n}^{1\alpha} \\ &= \left(\left(\mathbb{C}^1 - \mathbb{C}^\alpha\right)\left[\bar{\varepsilon} + \sum_{\gamma=2}^{\tilde{N}} \phi_\gamma (\boldsymbol{a}^{1\gamma}\otimes\boldsymbol{n}^{1\gamma})\right] + \mathbb{C}^\alpha\left[(\boldsymbol{a}^{1\alpha}\otimes\boldsymbol{n}^{1\alpha}) + \tilde{\boldsymbol{\varepsilon}}_0^\alpha + \tilde{\boldsymbol{\varepsilon}}_\mathrm{c}^\alpha\right] \right. \\ &\quad \left. - \mathbb{C}^1\left[\tilde{\boldsymbol{\varepsilon}}_0^1 + \tilde{\boldsymbol{\varepsilon}}_\mathrm{c}^1\right]\right)\boldsymbol{n}^{1\alpha}. \end{aligned} \tag{A.3}$$

The equal diffusion potential condition, which constitutes the third residual equation, cf. Eq. (44), is reformulated. Substituting Eqs. (50)–(51) and rearranging with the use of the definition of the strains yields

$$\begin{aligned} r_{\mu^\alpha} &= \frac{\partial f_\mathrm{el}^\alpha}{\partial c^\alpha} + \frac{\partial f_\mathrm{chem}^\alpha}{\partial c^\alpha} - \mu \\ &= -\tilde{\boldsymbol{\varepsilon}}_\mathrm{ref}^\alpha \cdot \left(\mathbb{C}^\alpha \left[\bar{\varepsilon} + \sum_{\gamma=2}^{\tilde{N}} \phi_\gamma \left(\boldsymbol{a}^{1\gamma}\otimes\boldsymbol{n}^{1\gamma}\right) - \left(1-\delta^{1\alpha}\right)\left(\boldsymbol{a}^{1\alpha}\otimes\boldsymbol{n}^{1\alpha}\right) \right.\right. \\ &\quad \left.\left. - \tilde{\boldsymbol{\varepsilon}}_0^\alpha - \tilde{\boldsymbol{\varepsilon}}_\mathrm{c}^\alpha \right]\right) + \frac{1}{V_\mathrm{m}}(2A^\alpha c^\alpha + B^\alpha) - \mu\,. \end{aligned} \tag{A.4}$$

Herein, $\delta^{1\alpha} = 1$ if $\alpha = 1$ and 0 otherwise.

For solving the system of equations, the partial derivatives of the residuals with respect to the unknowns have to be derived for the calculation of the Jacobian, cf. Eq. (45). The derivatives of the first residual equation, which is rearranged in Eq. (42), read

$$\frac{\partial r_c}{\partial c^\alpha} = \phi_\alpha \qquad \forall\,\alpha\in[1,\tilde{N}] \tag{A.5}$$

$$\frac{\partial r_c}{\partial \boldsymbol{a}^{1\alpha}} = \boldsymbol{0} \qquad \forall\,\alpha\in[2,\tilde{N}] \tag{A.6}$$

$$\frac{\partial r_c}{\partial \mu} = 0\,. \tag{A.7}$$

The derivatives of the second residual equation in Eq. (A.3) read

$$\frac{\partial \boldsymbol{r}_\sigma^{1\gamma}}{\partial c^\alpha} = -\left(\mathbb{C}^1\left[\tilde{\boldsymbol{\varepsilon}}_\mathrm{ref}^1\right]\right)\boldsymbol{n}^{1\gamma} \qquad \forall\,\gamma\in[2,\tilde{N}],\alpha=1 \tag{A.8}$$

$$\frac{\partial \boldsymbol{r}_\sigma^{1\gamma}}{\partial c^\alpha} = \delta^{\alpha\gamma}\left(\mathbb{C}^\alpha\left[\tilde{\boldsymbol{\varepsilon}}_\mathrm{ref}^\alpha\right]\right)\boldsymbol{n}^{1\gamma} \qquad \forall\,\alpha,\gamma\in[2,\tilde{N}] \tag{A.9}$$

$$\frac{\partial \boldsymbol{r}_\sigma^{1\gamma}}{\partial \boldsymbol{a}^{1\alpha}} = \left(\phi_\alpha[C_{ijkl}]^{1\gamma} + \delta^{\alpha\gamma}C_{ijkl}^\gamma\right) n_j^{1\gamma} n_l^{1\alpha}\boldsymbol{e}_i\otimes\boldsymbol{e}_k \qquad \forall\,\alpha,\gamma\in[2,\tilde{N}] \tag{A.10}$$

$$\frac{\partial \boldsymbol{r}_\sigma^{1\gamma}}{\partial \mu} = \boldsymbol{0} \qquad \forall\,\gamma\in[2,\tilde{N}]\,. \tag{A.11}$$

Herein, $\delta^{\alpha\gamma} = 1$ for $\alpha = \gamma$ and 0 otherwise. The derivatives of the third residual equation in Eq. (A.4) read

$$\frac{\partial r_\mu^\gamma}{\partial c^\alpha} = \delta^{\alpha\gamma}\left(\tilde{\boldsymbol{\varepsilon}}_\mathrm{ref}^\alpha\cdot\left(\mathbb{C}^\alpha\left[\tilde{\boldsymbol{\varepsilon}}_\mathrm{ref}^\alpha\right]\right) + \frac{2A^\alpha}{V_\mathrm{m}}\right) \qquad \forall\,\alpha,\gamma\in[1,\tilde{N}] \tag{A.12}$$

$$\frac{\partial r_\mu^\gamma}{\partial \boldsymbol{a}^{1\alpha}} = -(\phi_\alpha - \delta^{\alpha\gamma})\left(\mathbb{C}^\gamma\left[\tilde{\boldsymbol{\varepsilon}}_\mathrm{ref}^\gamma\right]\right)\boldsymbol{n}^{1\alpha} \qquad \forall\,\gamma\in[1,\tilde{N}],\ \alpha\in[2,\tilde{N}] \tag{A.13}$$

$$\frac{\partial r_\mu^\gamma}{\partial \mu} = -1 \qquad \forall\,\gamma\in[1,\tilde{N}]\,. \tag{A.14}$$

Appendix B. Implementation structure

This section provides an overview of the structure of the solver and the local problem. In this regard, flowcharts visualizing the structure are presented.

The proposed CMFC model is implemented in a modular manner. The structure of the solver is visualized in Fig. B.8. First, the evolution equation of the order parameters, cf. Eq. (9), and the evolution equation of the concentration, cf. Eq. (41), are solved explicitly. Second, the balance of linear momentum, cf. Eq. (30), is solved iteratively for the displacement. Upon identifying a displacement vector that solves the balance equation, the timestep is updated. In the event that the endtime has not yet been reached, the driving forces and fluxes are updated, and the subsequent solver iteration commences.

Within each iteration step, the local problem, defined in Eqs. (42)–(44), is solved for the phase-specific concentrations c^α, the

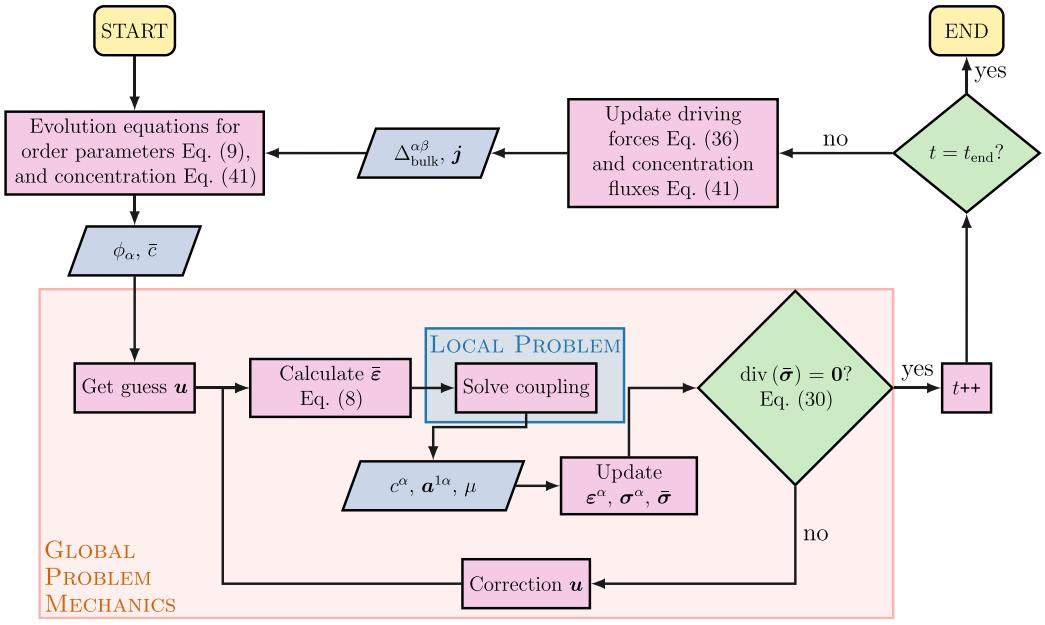

Fig. B.8. Structure of the solver. Firstly, evolution equations of order parameters and concentrations are solved. Secondly, the balance of linear momentum is solved iteratively for the displacement, while solving for the phase-specific concentration c^α, strain jump vectors $\boldsymbol{a}^{1\alpha}$, and the diffusion potential μ. Subsequently, the driving forces and fluxes are updated.

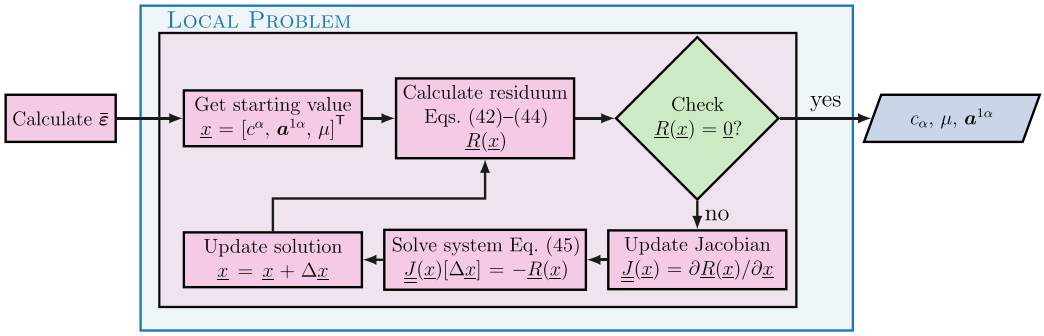

Fig. B.9. Structure of the implementation for solving the local problem. The local problem is solved employing a Newton routine.

strain jump vectors $\boldsymbol{a}^{1\alpha}$, and the diffusion potential μ. This is achieved through the use of a Newton routine. The structure of the local problem is visualized in Fig. B.9.

Appendix C. Remarks on the jump condition approach

The jump condition approach, as outlined by Schneider et al. [45] necessitates the selection of a reference phase, in regard to which the jump conditions are solved. In the following, the choice of the reference phase is discussed in detail.

In multiphase regions, i.e., regions with more than two phases, judicious selection of the reference phase is imperative. In this regard, a two-dimensional domain with a quadruple point, cf. Fig. C.10(a), is subjected to a periodic boundary condition that fulfills a macroscopic strain $\bar{\varepsilon} = 0.005 \boldsymbol{e}_\text{x} \otimes \boldsymbol{e}_\text{x}$, a similar validation setup is presented in [46]. The domain contains four phases with $E^\alpha = E^\beta/4 = E^\gamma/2 = E^\delta/3 = 50\,\text{GPa}$. In Fig. C.10, the impact of the choice of reference phase is further investigated. A sharp interface solution (referred to as SI) is produced with a sharp transition between order parameters. Three approaches are compared to this SI solution: In the first approach (RH), the phase with the highest phase fraction is identified and selected as the reference phase in each point in the diffuse interface area. For the second approach (RL), the phase with the lowest phase fraction is identified and selected as reference phase. In the third approach, each phase is chosen as reference phase iteratively, with subsequent averaging of the solutions, i.e., averaging of the resulting jump vectors $\boldsymbol{a}^{\text{R}\alpha}$. The resulting von Mises stress $\bar{\sigma}_\text{vM}$ Fig. C.10(b) and the elastic energy density $\bar{f}_\text{el}$ Fig. C.10(c) are compared along two diagonal paths across the quadruple point. The x-axes are colored to match the path's colors. The stress peaks of the SI solution are not reproduced by the diffuse interface approaches. However, the jump condition approach ensures a good agreement outside the diffuse interface area. The match is slightly worse, when the phase with the smallest phase fraction is chosen as reference. Moreover, numerical instabilities appear. The averaged approach is computationally more expensive and yields similar results to the approach, where the phase with the largest phase fraction is chosen as reference. Thus, the latter approach is chosen within this work. As argued in [46], the good match in the bulk region shows that the mechanical driving forces can be well reproduced even in a multiphase region.

Appendix D. Analytical solution to inclusion problem

The comparison scheme, which is employed in Section 4.2, utilizes a sharp interface mechanical boundary value problem, for which analytical solutions are required. Based on Eshelby's inclusion solution, cf. [95–97] a BVP is formulated and its analytical solutions are used for the benchmark in the work at hand. For the sake of completeness,

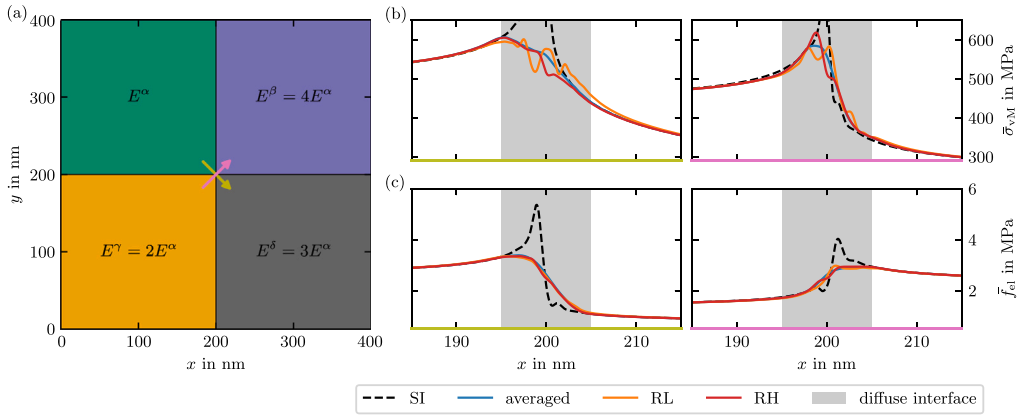

Fig. C.10. Validation of jump conditions in a quadruple point. A domain containing four phases with different elastic moduli (a) is subjected to a periodic boundary condition that fulfills a macroscopic strain. The resulting von Mises stress $\bar{\sigma}_{\mathrm{vM}}$ (b) and the elastic energy density $\bar{f}_{\mathrm{el}}$ (c) are plotted along two diagonal paths across the quadruple point as indicated by arrows in (a). A sharp interface (SI) solution is compared to solutions with different choice of reference phases: phase with highest volume fraction (RH), with the lowest volume fraction (RL), and an averaged solution, where each of the four phases is chosen as reference iteratively and the resulting solutions are averaged.

the stress $\boldsymbol{\sigma}$, strain $\boldsymbol{\varepsilon}$, and displacement fields $\boldsymbol{u}$ of the inclusion problem are reported below.

The analytical solutions to this two-dimensional BVP have been reported, e.g., by Li et al. [93] in terms of Eshelby tensors and equivalently by Fischer et al. [94] in terms of Airy stress functions. The superscript I refers to the solution fields inside of the inclusion and the superscript O to the solution fields outside of the inclusion. The radius of the circular inclusion is denoted by a. Isotropic inelastic strains $\tilde{\boldsymbol{\varepsilon}}^\alpha = \tilde{\varepsilon}^\alpha \boldsymbol{I}$, as defined in Eq. (52), are considered with $\tilde{\varepsilon}^\alpha = \tilde{\varepsilon}_0^\alpha + (c^\alpha - c_{\mathrm{ref}}^\alpha)\bar{\varepsilon}_{\mathrm{ref}}$. In what follows, the solution fields are expressed in a polar coordinate system with its origin in the center of the inclusion, as visualized in Fig. 2. The displacement fields read

$$\boldsymbol{u}^{\mathrm{I}} = -\frac{\tilde{\varepsilon}^\alpha}{2(\nu-1)} r \boldsymbol{e}_{\mathrm{r}} \tag{D.1}$$

$$\boldsymbol{u}^{\mathrm{O}} = -\frac{\tilde{\varepsilon}^\alpha}{2(\nu-1)} \frac{a^2}{r} \boldsymbol{e}_{\mathrm{r}} \,. \tag{D.2}$$

A parametrization along the boundary of a quadratic domain yields the Dirichlet boundary conditions employing $\boldsymbol{u}^{\mathrm{O}}$. Furthermore, for the formulation of the mechanical driving force $\Delta^{\alpha\beta}_{\mathrm{mech}}$ it is necessary to derive the stress and strain fields. The resulting stress fields read

$$\boldsymbol{\sigma}^{\mathrm{I}} = \frac{E\tilde{\varepsilon}^\alpha}{2(\nu^2-1)} \left(\boldsymbol{e}_{\mathrm{r}} \otimes \boldsymbol{e}_{\mathrm{r}} + \boldsymbol{e}_\theta \otimes \boldsymbol{e}_\theta\right) \tag{D.3}$$

$$\boldsymbol{\sigma}^{\mathrm{O}} = \frac{E\tilde{\varepsilon}^\alpha}{2(\nu^2-1)} \frac{a^2}{r^2} \left(\boldsymbol{e}_{\mathrm{r}} \otimes \boldsymbol{e}_{\mathrm{r}} - \boldsymbol{e}_\theta \otimes \boldsymbol{e}_\theta\right) . \tag{D.4}$$

The elastic strain fields are derived with the assumption of an isotropic stiffness with

$$\boldsymbol{\varepsilon}_{\mathrm{el}} = \frac{1+\nu}{E}\left(\boldsymbol{\sigma} - \frac{\nu}{1+\nu}\mathrm{tr}(\boldsymbol{\sigma})\boldsymbol{I}\right) , \tag{D.5}$$

cf., e.g., [100, Eq. (4.1.18)] and assuming plane strain conditions arise as

$$\boldsymbol{\varepsilon}_{\mathrm{el}}^{\mathrm{I}} = \frac{(1-2\nu)\tilde{\varepsilon}^\alpha}{2(\nu-1)} \left(\boldsymbol{e}_{\mathrm{r}} \otimes \boldsymbol{e}_{\mathrm{r}} + \boldsymbol{e}_\theta \otimes \boldsymbol{e}_\theta\right) \tag{D.6}$$

$$\boldsymbol{\varepsilon}_{\mathrm{el}}^{\mathrm{O}} = \frac{\tilde{\varepsilon}^\alpha}{2(\nu-1)} \frac{a^2}{r^2} \left(\boldsymbol{e}_{\mathrm{r}} \otimes \boldsymbol{e}_{\mathrm{r}} - \boldsymbol{e}_\theta \otimes \boldsymbol{e}_\theta\right) . \tag{D.7}$$

Appendix E. Equilibrium conditions for the described BVP

In this section, the driving forces used in Section 4.2 are reported in detail. In this single inclusion setup, the phase α is considered in the inclusion, while the phase β is present in the surrounding matrix.

The chemical driving force is derived by substituting Eq. (49) in Eq. (47) and reads

$$\begin{aligned}\Delta^{\alpha\beta}_{\mathrm{chem}} &= \{f_{\mathrm{chem}}\}^{\alpha\beta} - \mu^\alpha_{\mathrm{chem}}\{c\}^{\alpha\beta} \\ &= \frac{\left(A^\alpha (c^\alpha)^2 + B^\alpha c^\alpha + C^\alpha\right) - \left(A^\beta (c^\beta)^2 + B^\beta c^\beta + C^\beta\right)}{V_{\mathrm{m}}} \\ &\quad - \left(\frac{2A^\alpha c^\alpha + B^\alpha}{V_{\mathrm{m}}}\right)\left(c^\alpha - c^\beta\right) .\end{aligned} \tag{E.1}$$

It is the same for all coupling approaches. The capillary driving force is derived by substituting an expression for the curvature of the interface between inclusion α and matrix β in terms of the concentrations c^α and c^β. As delineated in [68], the mean curvature can be expressed as

$$\bar{\kappa}_S(c^\alpha, c^\beta) = \frac{1}{2a(c^\alpha, c^\beta)} = \frac{1}{2}\left(\frac{|c_{\mathrm{tot}} - c^\beta|}{|c^\alpha - c^\beta|}\frac{A_{\mathrm{tot}}}{\pi}\right)^{-\frac{1}{2}} . \tag{E.2}$$

Herein, a denotes the radius of the circular inclusion. In conclusion, the capillary driving force in Eq. (47) for all coupling approaches reads

$$\Delta^{\alpha\beta}_{\mathrm{cap}} = 2\gamma_{\alpha\beta}\bar{\kappa}_S = \gamma_{\alpha\beta}\left(\frac{|c_{\mathrm{tot}} - c^\beta| A_{\mathrm{tot}}}{|c^\alpha - c^\beta|\pi}\right)^{-\frac{1}{2}} . \tag{E.3}$$

The mechanical driving force $\Delta^{\alpha\beta}_{\mathrm{mech}}$ at the corresponding sharp interface between phase α and β as defined in Eq. (47) for the CMFC model is given by

$$\begin{aligned}\Delta^{\alpha\beta}_{\mathrm{mech}} &= \{f_{\mathrm{el}}\}^{\alpha\beta} - \bar{\boldsymbol{\sigma}} \cdot \{\boldsymbol{\varepsilon}\}^{\alpha\beta} - \mu^\alpha_{\mathrm{el}}\{c\}^{\alpha\beta} \\ &= \frac{1}{2}\left(\boldsymbol{\varepsilon}^\alpha_{\mathrm{el}} \cdot \boldsymbol{\sigma}^\alpha - \boldsymbol{\varepsilon}^\beta_{\mathrm{el}} \cdot \boldsymbol{\sigma}^\beta\right) \\ &\quad - \frac{1}{2}\left(\boldsymbol{\sigma}^\alpha + \boldsymbol{\sigma}^\beta\right) \cdot \left(\boldsymbol{\varepsilon}^\alpha_{\mathrm{el}} + \tilde{\varepsilon}^\alpha \boldsymbol{I} - \boldsymbol{\varepsilon}^\beta_{\mathrm{el}} - \tilde{\varepsilon}^\beta \boldsymbol{I}\right) \\ &\quad + \{c\}^{\alpha\beta}\tilde{\varepsilon}^\alpha_{\mathrm{ref}}\mathrm{tr}(\boldsymbol{\sigma}^\alpha)\end{aligned} \tag{E.4}$$

$$= \frac{-E(\tilde{\varepsilon}^\alpha)^2 + 2\tilde{\varepsilon}^\alpha_{\mathrm{ref}} E\tilde{\varepsilon}^\alpha (c^\alpha - c^\beta)}{2(\nu^2-1)} . \tag{E.5}$$

Herein, the mean stress is computed as $\bar{\boldsymbol{\sigma}} = (\boldsymbol{\sigma}^\alpha + \boldsymbol{\sigma}^\beta)/2$, as defined in the sharp interface context [41, p. 32] and the analytical solutions as given in Appendix D are substituted. Using the CMWC or CMOC model, the mechanical diffusion potential μ^α_{el} vanishes or is neglected, thus with these models the mechanical driving force reduces to

$$\Delta^{\alpha\beta}_{\mathrm{mech}} = \{f_{\mathrm{el}}\}^{\alpha\beta} - \bar{\boldsymbol{\sigma}} \cdot \{\boldsymbol{\varepsilon}\}^{\alpha\beta} = \frac{-E(\tilde{\varepsilon}^\alpha)^2}{2(\nu^2-1)} . \tag{E.6}$$

Furthermore, with a CMWC model, no concentration dependent eigenstrains are considered. In this case, $\tilde{\varepsilon}^\alpha = \tilde{\varepsilon}^\alpha_0$ is assumed. In conclusion,

Table F.5
Details on a numerical investigation of a CMFC 2D diffusion example. An increase in mesh density with decreasing spacial discretization causes an increase in CPU time which is approximately inversely proportional to $(\Delta x)^2$. While the average number of global Newton iterations increases the proportion of cells in the interface decreases.

Spacial discretization Δx	2.50 nm	2.00 nm	1.67 nm
Total number of cells	6400	10000	14400
Ratio $t_{\mathrm{CPU}}/(\Delta x)^{-2}$	3473.78 s nm^2	3616.40 s nm^2	3714.71 s nm^2
Proportion of cells in interface	29.36 %	24.08 %	20.23 %
Average number of global Newton iterations	1.340	1.403	1.799

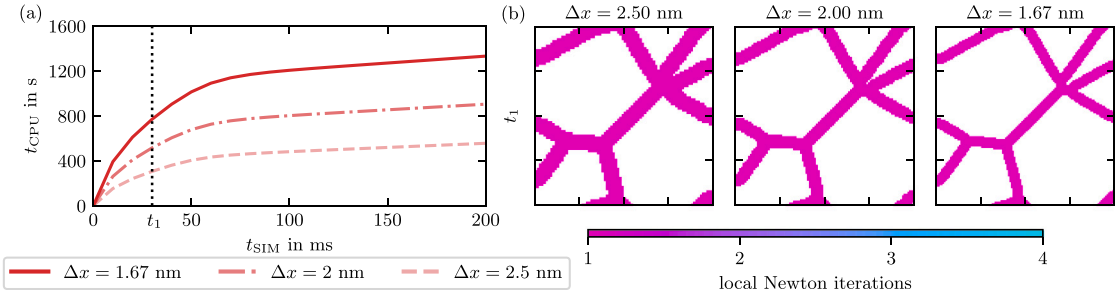

Fig. F.11. Numerical investigation of a CMFC 2D diffusion example. In (a), the CPU times t_{CPU} are plotted against the simulation time t_{SIM} for different spatial discretizations Δx, i.e., different total numbers of grid points. The increase in CPU time due to the increased number of grid points is approximately inversely proportional to $(\Delta x)^2$. In (b), the local Newton steps needed in the CMFC model are plotted for time t_1.

the equilibrium conditions for a CMFC model read

$$g_1^{\mathrm{CMFC}}(c^\alpha, c^\beta) := \frac{\left(A^\alpha (c^\alpha)^2 + B^\alpha c^\alpha + C^\alpha\right) - \left(A^\beta (c^\beta)^2 + B^\beta c^\beta + C^\beta\right)}{V_{\mathrm{m}}} - \left(\frac{2A^\alpha c^\alpha + B^\alpha}{V_{\mathrm{m}}} + \frac{\tilde{\varepsilon}^\alpha_{\mathrm{ref}} E \left(\varepsilon_0^\alpha + \tilde{\varepsilon}^\alpha_{\mathrm{ref}}(c^\alpha - c^\alpha_{\mathrm{ref}})\right)}{1-\nu^2} \right)(c^\alpha - c^\beta) - \frac{E\left(\varepsilon_0^\alpha + \tilde{\varepsilon}^\alpha_{\mathrm{ref}}(c^\alpha - c^\alpha_{\mathrm{ref}})\right)^2}{2(\nu^2-1)} + \gamma_{\alpha\beta}\left(\frac{|c_{\mathrm{tot}} - c^\beta| A_{\mathrm{tot}}}{|c^\alpha - c^\beta|\pi}\right)^{-1/2} = 0 \tag{E.7}$$

$$g_2^{\mathrm{CMFC}}(c^\alpha, c^\beta) := \frac{2A^\alpha c^\alpha + B^\alpha}{V_{\mathrm{m}}} + \tilde{\varepsilon}^\alpha_{\mathrm{ref}} E \frac{\varepsilon_0^\alpha + \tilde{\varepsilon}^\alpha_{\mathrm{ref}}(c^\alpha - c^\alpha_{\mathrm{ref}})}{1-\nu^2} - \frac{2A^\beta c^\beta + B^\beta}{V_{\mathrm{m}}} = 0\,. \tag{E.8}$$

The equilibrium conditions for a CMOC model read

$$g_1^{\mathrm{CMOC}}(c^\alpha, c^\beta) := \frac{\left(A^\alpha (c^\alpha)^2 + B^\alpha c^\alpha + C^\alpha\right) - \left(A^\beta (c^\beta)^2 + B^\beta c^\beta + C^\beta\right)}{V_{\mathrm{m}}} - \left(\frac{2A^\alpha c^\alpha + B^\alpha}{V_{\mathrm{m}}} \right)(c^\alpha - c^\beta) - \frac{E\left(\varepsilon_0^\alpha + \tilde{\varepsilon}^\alpha_{\mathrm{ref}}(c^\alpha - c^\alpha_{\mathrm{ref}})\right)^2}{2(\nu^2-1)} + \gamma_{\alpha\beta}\left(\frac{|c_{\mathrm{tot}} - c^\beta| A_{\mathrm{tot}}}{|c^\alpha - c^\beta|\pi}\right)^{-1/2} = 0 \tag{E.9}$$

$$g_2^{\mathrm{CMOC}}(c^\alpha, c^\beta) := \frac{2A^\alpha c^\alpha + B^\alpha}{V_{\mathrm{m}}} - \frac{2A^\beta c^\beta + B^\beta}{V_{\mathrm{m}}} = 0\,. \tag{E.10}$$

And finally, the equilibrium conditions for a CMWC model read

$$g_1^{\mathrm{CMWC}}(c^\alpha, c^\beta) := \frac{\left(A^\alpha (c^\alpha)^2 + B^\alpha c^\alpha + C^\alpha\right) - \left(A^\beta (c^\beta)^2 + B^\beta c^\beta + C^\beta\right)}{V_{\mathrm{m}}} - \left(\frac{2A^\alpha c^\alpha + B^\alpha}{V_{\mathrm{m}}} \right)(c^\alpha - c^\beta) - \frac{E(\varepsilon_0^\alpha)^2}{2(\nu^2-1)} + \gamma_{\alpha\beta}\left(\frac{|c_{\mathrm{tot}} - c^\beta| A_{\mathrm{tot}}}{|c^\alpha - c^\beta|\pi}\right)^{-1/2} = 0 \tag{E.11}$$

$$g_2^{\mathrm{CMWC}}(c^\alpha, c^\beta) := \frac{2A^\alpha c^\alpha + B^\alpha}{V_{\mathrm{m}}} - \frac{2A^\beta c^\beta + B^\beta}{V_{\mathrm{m}}} = 0\,. \tag{E.12}$$

Appendix F. Numerical investigation

In this section, the 2D diffusion example presented in Section 4.4 is investigated regarding numerical aspects. The CPU times t_{CPU} are compared for different spatial discretizations Δx, i.e., different total numbers of grid points.

In Fig. F.11(a), the CPU time t_{CPU} is plotted against the simulation time t_{SIM}. With the CMFC model, the number of necessitated global Newton iterations increases with increased number of grid points, but the proportion of cells in the interface decreases due to the constant number of grid points in the interface, cf. Table F.5. The thickness of the interface is eight times the spacial discretization which is common in phase-field methods, cf., e.g., [101]. In consequence, the CPU time t_{CPU} is approximately inversely proportional to $(\Delta x)^2$. For time t_1, the local Newton steps needed to solve Eq. (45) in the CMFC model are plotted in Fig. F.11(b). Accounting for a constant stiffness tensor and Eq. (38) and Eq. (51), the local system Eq. (45) becomes linear. Consequently, the corresponding Jacobian is constant with respect to the unknowns, cf. Eqs. (A.5)–(A.14). As a result, the local system can be solved in the first iteration step as reflected in Fig. F.11(b).

Data availability

Data will be made available on request.

References

[1] Song Y, Shao X, Guo Z, Zhang J. Role of material properties and mechanical constraint on stress-assisted diffusion in plate electrodes of lithium ion batteries. J Phys D: Appl Phys 2013;46(10):105307. http://dx.doi.org/10.1088/0022-3727/46/10/105307.

[2] Wang Y, Li J, Ma S, Zhao M, Dai C, Zhao L, et al. A multi-scale heterogeneous electrochemical-diffusion-induced stress coupling model for lithium-ion batteries. J Electrochem Soc 2022;169(10):100524. http://dx.doi.org/10.1149/1945-7111/ac964d.

[3] Martínez-Pañeda E, Golahmar A, Niordson CF. A phase field formulation for hydrogen assisted cracking. Comput Methods Appl Mech Engrg 2018;342:742–61. http://dx.doi.org/10.1016/j.cma.2018.07.021.

[4] Bai Y, Mianroodi JR, Ma Y, da Silva AK, Svendsen B, Raabe D. Chemo-mechanical phase-field modeling of iron oxide reduction with hydrogen. Acta Mater 2022;231:117899. http://dx.doi.org/10.1016/j.actamat.2022.117899.

[5] Cahn JW, Hilliard JE. Free energy of a nonuniform system. I. Interfacial free energy. J Chem Phys 1958;28(2):258–67. http://dx.doi.org/10.1063/1.1744102.

[6] Ginzburg VL. On the theory of superconductivity. Il Nuovo Cimento 1955;2(6):1234–50. http://dx.doi.org/10.1007/BF02731579.

[7] Cahn J, Larché F. A simple model for coherent equilibrium. Acta Metall 1984;32(11):1915–23. http://dx.doi.org/10.1016/0001-6160(84)90173-1.

[8] Chen L-Q. Phase-field models for microstructure evolution. Annu Rev Mater Res 2002;32(1):113–40. http://dx.doi.org/10.1146/annurev.matsci.32.112001.132041.

[9] Moelans N, Blanpain B, Wollants P. An introduction to phase-field modeling of microstructure evolution. Calphad 2008;32(2):268–94. http://dx.doi.org/10.1016/j.calphad.2007.11.003.

[10] Steinbach I. Phase-field models in materials science. Modelling Simul Mater Sci Eng 2009;17(7):073001. http://dx.doi.org/10.1088/0965-0393/17/7/073001.

[11] Tourret D, Liu H, LLorca J. Phase-field modeling of microstructure evolution: Recent applications, perspectives and challenges. Prog Mater Sci 2022;123:100810. http://dx.doi.org/10.1016/j.pmatsci.2021.100810.

[12] Li P, Li W, Li B, Yang S, Shen Y, Wang Q, et al. A review on phase field models for fracture and fatigue. Eng Fract Mech 2023;289:109419. http://dx.doi.org/10.1016/j.engfracmech.2023.109419.

[13] Yamanaka A. Phase-field modeling and simulation of solid-state phase transformations in steels. ISIJ Int 2023;63(3):395–406. http://dx.doi.org/10.2355/isijinternational.ISIJINT-2022-343.

[14] Hong L, Yang K, Tang M. A mechanism of defect-enhanced phase transformation kinetics in lithium iron phosphate olivine. Npj Comput Mater 2019;5(1):118. http://dx.doi.org/10.1038/s41524-019-0255-3.

[15] Daubner S, Dillenz M, Pfeiffer LF, Gauckler C, Rosin M, Burgard N, et al. Combined study of phase transitions in the P2-type NaXNi1/3Mn2/3O2 cathode material: experimental, ab-initio and multiphase-field results. Npj Comput Mater 2024;10(1). http://dx.doi.org/10.1038/s41524-024-01258-x.

[16] Weichel M, Reder M, Daubner S, Klemens J, Burger D, Scharfer P, et al. Modeling the drying process in hard carbon electrodes based on the phase-field method. Phys Rev Mater 2025;9(3):035403. http://dx.doi.org/10.1103/PhysRevMaterials.9.035403.

[17] Radice E, Salvalaglio M, Bergamaschini R. Phase-field modelling of anisotropic solid-state dewetting on patterned substrates. Acta Mater 2025;292:120992. http://dx.doi.org/10.1016/j.actamat.2025.120992.

[18] Verma M, Mukherjee R. Nanoparticle formation through dewetting of a solid-state thin film on a substrate: A phase-field study. J Alloys Compd 2020;835:155163. http://dx.doi.org/10.1016/j.jallcom.2020.155163.

[19] Eiken J, Böttger B, Apel M. Diffuse modelling of pearlite growth in calphad-coupled multicomponent multi-phase-field simulations. IOP Conf Ser: Mater Sci Eng 2023;1281(1):012051. http://dx.doi.org/10.1088/1757-899X/1281/1/012051.

[20] Salama H, Ali MA, Shchyglo O, Steinbach I. Phase-field simulation framework for modeling martensite and bainite formation in steel. Comput Mater Sci 2024;241:113033. http://dx.doi.org/10.1016/j.commatsci.2024.113033.

[21] Ruan H, Rezaei S, Yang Y, Gross D, Xu B-X. A thermo-mechanical phase-field fracture model: Application to hot cracking simulations in additive manufacturing. J Mech Phys Solids 2023;172:105169. http://dx.doi.org/10.1016/j.jmps.2022.105169.

[22] Elmoghazy A, Heuer A, Kneer A, Reder M, Prahs A, Schneider D, et al. Phase-field modeling of the morphological and thermal evolution of additively manufactured polylactic acid layers and their influence on the effective elastic mechanical properties. Prog Addit Manuf 2024. http://dx.doi.org/10.1007/s40964-024-00891-8.

[23] Dammaß F, Kalina KA, Ambati M, Kästner M. Phase-field modelling and analysis of rate-dependent fracture phenomena at finite deformation. Comput Mech 2023;72(5):859–83. http://dx.doi.org/10.1007/s00466-023-02310-1.

[24] Henry H. Pinning of crack fronts by hard and soft inclusions: A phase field study. Phys Rev E 2024;109(2):025002. http://dx.doi.org/10.1103/PhysRevE.109.025002.

[25] Baktheer A, Martínez-Pañeda E, Aldakheel F. Phase field cohesive zone modeling for fatigue crack propagation in quasi-brittle materials. Comput Methods Appl Mech Engrg 2024;422:116834. http://dx.doi.org/10.1016/j.cma.2024.116834.

[26] Kobayashi R. Modeling and numerical simulations of dendritic crystal growth. Phys D: Nonlinear Phenom 1993;63(3–4):410–23. http://dx.doi.org/10.1016/0167-2789(93)90120-p.

[27] Zhang A, Guo Z, Jiang B, Xiong S, Pan F. Numerical solution to phase-field model of solidification: A review. Comput Mater Sci 2023;228:112366. http://dx.doi.org/10.1016/j.commatsci.2023.112366.

[28] Umar M, Seiz M, Kellner M, Nestler B, Schneider D. Solidification of a quaternary X5CrNi18-10 alloy during laser beam welding using CALPHAD data in a phase-field approach. Comput Mater Sci 2025;249:113627. http://dx.doi.org/10.5445/IR/1000178958.

[29] Wheeler AA, Boettinger WJ, McFadden GB. Phase-field model for isothermal phase transitions in binary alloys. Phys Rev A 1992;45(10):7424–39. http://dx.doi.org/10.1103/physreva.45.7424.

[30] Kim SG, Kim WT, Suzuki T. Phase-field model for binary alloys. Phys Rev E 1999;60(6):7186–97. http://dx.doi.org/10.1103/physreve.60.7186.

[31] Tiaden J, Nestler B, Diepers HJ, Steinbach I. The multiphase-field model with an integrated concept for modelling solute diffusion. Phys D: Nonlinear Phenom 1998;115(1–2):73–86. http://dx.doi.org/10.1016/S0167-2789(97)00226-1.

[32] Plapp M. Unified derivation of phase-field models for alloy solidification from a grand-potential functional. Phys Rev E 2011;84(3):031601. http://dx.doi.org/10.1103/physreve.84.031601.

[33] Choudhury A, Nestler B. Grand-potential formulation for multicomponent phase transformations combined with thin-interface asymptotics of the double-obstacle potential. Phys Rev E 2012;85(2):021602. http://dx.doi.org/10.1103/physreve.85.021602.

[34] Ammar K, Appolaire B, Cailletaud G, Forest S. Combining phase field approach and homogenization methods for modelling phase transformation in elastoplastic media. Eur J Comput Mech 2009;18(5–6):485–523. http://dx.doi.org/10.3166/ejcm.18.485-523.

[35] Khachaturyan AG. Theory of structural transformations in solids. New York: John Wiley & Sons, Inc.; 1983.

[36] Steinbach I, Apel M. Multi phase field model for solid state transformation with elastic strain. Phys D: Nonlinear Phenom 2006;217(2):153–60. http://dx.doi.org/10.1016/j.physd.2006.04.001.

[37] Steinbach I, Apel M. The influence of lattice strain on pearlite formation in Fe–C. Acta Mater 2007;55(14):4817–22. http://dx.doi.org/10.1016/j.actamat.2007.05.013.

[38] Schneider D, Tschukin O, Choudhury A, Selzer M, Böhlke T, Nestler B. Phase-field elasticity model based on mechanical jump conditions. Comput Mech 2015;55(5):887–901. http://dx.doi.org/10.1007/s00466-015-1141-6.

[39] Durga A, Wollants P, Moelans N. Evaluation of interfacial excess contributions in different phase-field models for elastically inhomogeneous systems. Modelling Simul Mater Sci Eng 2013;21(5):055018. http://dx.doi.org/10.1088/0965-0393/21/5/055018.

[40] Mosler J, Shchyglo O, Hojjat HM. A novel homogenization method for phase field approaches based on partial rank-one relaxation. J Mech Phys Solids 2014;68:251–66. http://dx.doi.org/10.1016/j.jmps.2014.04.002.

[41] Silhavy M. The mechanics and thermodynamics of continuous media. Berlin, Heidelberg: Springer; 1997, p. 504.

[42] Durga A, Wollants P, Moelans N. A quantitative phase-field model for two-phase elastically inhomogeneous systems. Comput Mater Sci 2015;99:81–95. http://dx.doi.org/10.1016/j.commatsci.2014.11.057.

[43] Durga A, Wollants P, Moelans N. Phase-field study of IMC growth in Sn–Cu/Cu solder joints including elastoplastic effects. Acta Mater 2020;188:241–58. http://dx.doi.org/10.1016/j.actamat.2020.01.052.

[44] Kiefer B, Furlan T, Mosler J. A numerical convergence study regarding homogenization assumptions in phase field modeling. Internat J Numer Methods Engrg 2017;112(9):1097–128. http://dx.doi.org/10.1002/nme.5547.

[45] Schneider D, Schwab F, Schoof E, Reiter A, Herrmann C, Selzer M, et al. On the stress calculation within phase-field approaches: a model for finite deformations. Comput Mech 2017;60(2):203–17. http://dx.doi.org/10.1007/s00466-017-1401-8.

[46] Schneider D, Schoof E, Tschukin O, Reiter A, Herrmann C, Schwab F, et al. Small strain multiphase-field model accounting for configurational forces and mechanical jump conditions. Comput Mech 2017;61(3):277–95. http://dx.doi.org/10.1007/s00466-017-1458-4.

[47] Schoof E, Schneider D, Streichhan N, Mittnacht T, Selzer M, Nestler B. Multiphase-field modeling of martensitic phase transformation in a dual-phase microstructure. Int J Solids Struct 2018;134:181–94. http://dx.doi.org/10.1016/j.ijsolstr.2017.10.032.

[48] Amos PGK, Schoof E, Schneider D, Nestler B. Chemo-elastic phase-field simulation of the cooperative growth of mutually-accommodating Widmanstätten plates. J Alloys Compd 2018;767:1141–54. http://dx.doi.org/10.1016/j.jallcom.2018.07.138.

[49] Schoof E, Amos PGK, Schneider D, Nestler B. Influence of stress-free transformation strain on the autocatalytic growth of bainite: A multiphase-field analysis. Materialia 2020;9:100620. http://dx.doi.org/10.1016/j.mtla.2020.100620.

[50] Schöller L, Schneider D, Prahs A, Nestler B. Phase-field modeling of crack propagation based on multi-crack order parameters considering mechanical jump conditions. PAMM 2023;22(1):e202200039. http://dx.doi.org/10.1002/pamm.202200039.

[51] Reder M, Prahs A, Schneider D, Nestler B. Viscous stress approximations in diffuse interface methods for two-phase flow based on mechanical jump conditions. Comput Methods Appl Mech Engrg 2024;432:117341. http://dx.doi.org/10.1016/j.cma.2024.117341.

[52] Prahs A, Reder M, Schneider D, Nestler B. Thermomechanically coupled theory in the context of the multiphase-field method. Int J Mech Sci 2023;257:108484. http://dx.doi.org/10.1016/j.ijmecsci.2023.108484.

[53] Prahs A, Schneider D, Nestler B. A continuum thermodynamic approach to the phase-field method: The order parameter as internal state variable. Contin Mech Thermodyn 2025;37(4):55. http://dx.doi.org/10.1007/s00161-025-01383-y.

[54] Larché F, Cahn J. A linear theory of thermochemical equilibrium of solids under stress. Acta Metall 1973;21(8):1051–63. http://dx.doi.org/10.1016/0001-6160(73)90021-7.

[55] Larché F, Cahn JW. A nonlinear theory of thermochemical equilibrium of solids under stress. Acta Metall 1978;26(1):53–60. http://dx.doi.org/10.1016/0001-6160(78)90201-8.

[56] Böttger B, Apel M, Budnitzki M, Eiken J, Laschet G, Zhou B. Calphad coupled phase-field model with mechano-chemical contributions and its application to rafting of γ' in CMSX-4. Comput Mater Sci 2020;184:109909. http://dx.doi.org/10.1016/j.commatsci.2020.109909.

[57] Svendsen B, Shanthraj P, Raabe D. Finite-deformation phase-field chemo-mechanics for multiphase, multicomponent solids. J Mech Phys Solids 2018;112:619–36. http://dx.doi.org/10.1016/j.jmps.2017.10.005.

[58] Tschukin O, Schneider D, Nestler B. An elasto-chemical phase-field model for isotropic solids. Eur J Mech A Solids 2019;73:181–91. http://dx.doi.org/10.1016/j.euromechsol.2018.06.014.

[59] Simon P-CA, Aagesen LK, Motta AT, Tonks MR. The effects of introducing elasticity using different interpolation schemes to the grand potential phase field model. Comput Mater Sci 2020;183:109790. http://dx.doi.org/10.1016/j.commatsci.2020.109790.

[60] Kamachali RD, Borukhovich E, Shchyglo O, Steinbach I. Solutal gradients in strained equilibrium. Phil Mag Lett 2013;93(12):680–7. http://dx.doi.org/10.1080/09500839.2013.847288.

[61] Kamachali RD, Schwarze C, Lin M, Diehl M, Shanthraj P, Prahl U, et al. Numerical benchmark of phase-field simulations with elastic strains: Precipitation in the presence of chemo-mechanical coupling. Comput Mater Sci 2018;155:541–53. http://dx.doi.org/10.1016/j.commatsci.2018.09.011.

[62] Chatterjee S, Schwen D, Moelans N. An efficient and quantitative phase-field model for elastically heterogeneous two-phase solids based on a partial rank-one homogenization scheme. Int J Solids Struct 2022;250:111709. http://dx.doi.org/10.1016/j.ijsolstr.2022.111709.

[63] Chatterjee S, Schwen D, Moelans N. A computationally efficient and mechanically compatible multi-phase-field model applied to coherently stressed three-phase solids. Comput Mater Sci 2023;218:111969. http://dx.doi.org/10.1016/j.commatsci.2022.111969.

[64] Shanthraj P, Liu C, Akbarian A, Svendsen B, Raabe D. Multi-component chemo-mechanics based on transport relations for the chemical potential. Comput Methods Appl Mech Engrg 2020;365:113029. http://dx.doi.org/10.1016/j.cma.2020.113029.

[65] Bartels A, Kurzeja P, Mosler J. Cahn–hilliard phase field theory coupled to mechanics: Fundamentals, numerical implementation and application to topology optimization. Comput Methods Appl Mech Engrg 2021;383:113918. http://dx.doi.org/10.1016/j.cma.2021.113918.

[66] Dyck A, Gisy J, Hille F, Wagner S, Pundt A, Böhlke T. Hydride formation in open thin film metal hydrogen systems: Cahn–Hilliard-type phase-field simulations coupled to elasto-plastic deformations. Mech Mater 2025;203:105258. http://dx.doi.org/10.1016/j.mechmat.2025.105258.

[67] Daubner S, Amos PGK, Schoof E, Santoki J, Schneider D, Nestler B. Multiphase-field modeling of spinodal decomposition during intercalation in an Allen-Cahn framework. Phys Rev Mater 2021;5(3):035406. http://dx.doi.org/10.1103/PhysRevMaterials.5.035406.

[68] Kannenberg T, Prahs A, Svendsen B, Nestler B, Schneider D. Chemo-mechanical benchmark for phase-field approaches. Modelling Simul Mater Sci Eng 2025;33(1):015004. http://dx.doi.org/10.1088/1361-651X/ad90f7.

[69] Nestler B, Garcke H, Stinner B. Multicomponent alloy solidification: Phase-field modeling and simulations. Phys Rev E 2005;71(4):041609. http://dx.doi.org/10.1103/physreve.71.041609.

[70] Steinbach I, Pezzolla F. A generalized field method for multiphase transformations using interface fields. Phys D: Nonlinear Phenom 1999;134(4):385–93. http://dx.doi.org/10.1016/s0167-2789(99)00129-3.

[71] Hoffrogge PW, Daubner S, Schneider D, Nestler B, Zhou B, Eiken J. Triple junction benchmark for multiphase-field models combining capillary and bulk driving forces. Modelling Simul Mater Sci Eng 2025;33(1):015001. http://dx.doi.org/10.1088/1361-651X/ad8d6f.

[72] Goldstein H, Poole CP, Safko JL. Classical mechanics. 3rd ed. San Francisco: Addison Wesley; 2002, p. 680.

[73] Larche FC, Cahn JW. The interactions of composition and stress in crystalline solids. J Res Natl Bur Stand 1984;89(6):467. http://dx.doi.org/10.6028/jres.089.026.

[74] Voorhees PW, Johnson WC. The thermodynamics of elastically stressed crystals. In: Solid state physics, vol. 59, Elsevier; 2004, p. 1–201. http://dx.doi.org/10.1016/S0081-1947(04)80003-1.

[75] Eiken J, Böttger B, Steinbach I. Multiphase-field approach for multicomponent alloys with extrapolation scheme for numerical application. Phys Rev E 2006;73(6):066122. http://dx.doi.org/10.1103/physreve.73.066122.

[76] Hoffrogge PW, Mukherjee A, Nani ES, Amos PGK, Wang F, Schneider D, et al. Multiphase-field model for surface diffusion and attachment kinetics in the grand-potential framework. Phys Rev E 2021;103(3):033307. http://dx.doi.org/10.1103/physreve.103.033307.

[77] Daubner S. modeling battery intercalation materials with the multiphase-field method (Ph.D. thesis), Karlsruher Institut für Technologie (KIT); 2023, http://dx.doi.org/10.5445/IR/1000164858.

[78] Prahs A, Schöller L, Schwab FK, Schneider D, Böhlke T, Nestler B. A multiphase-field approach to small strain crystal plasticity accounting for balance equations on singular surfaces. Comput Mech 2023;73. http://dx.doi.org/10.1007/s00466-023-02389-6.

[79] Kannenberg T, Schöller L, Prahs A, Schneider D, Nestler B. Investigation of microstructure evolution accounting for crystal plasticity in the multiphase-field method. PAMM 2023;23(3):e202300138. http://dx.doi.org/10.1002/pamm.202300138.

[80] Kannenberg T, Schöller L, Prahs A, Schneider D, Nestler B. Microstructure evolution accounting for crystal plasticity in the context of the multiphase-field method. Comput Mech 2024;74(1):67–84. http://dx.doi.org/10.1007/s00466-023-02423-7.

[81] Wu CH. The role of eshelby stress in composition-generated and stress-assisted diffusion. J Mech Phys Solids 2001;49(8):1771–94. http://dx.doi.org/10.1016/S0022-5096(01)00011-4.

[82] Vegard L. Die Konstitution der Mischkristalle und die Raumfüllung der Atome. Z Phys 1921;5(1):17–26. http://dx.doi.org/10.1007/BF01349680.

[83] Gottstein G. Physical foundations of materials science. Berlin: Springer Berlin Heidelberg; 2004, p. 502.

[84] Amos PGK, Schoof E, Streichan N, Schneider D, Nestler B. Phase-field analysis of quenching and partitioning in a polycrystalline Fe-C system under constrained-carbon equilibrium condition. Comput Mater Sci 2019;159:281–96. http://dx.doi.org/10.1016/j.commatsci.2018.12.023.

[85] Johnson WC, Alexander JID. Interfacial conditions for thermomechanical equilibrium in two-phase crystals. J Appl Phys 1986;59(8):2735–46. http://dx.doi.org/10.1063/1.336982.

[86] Voorhees PW, Johnson WC. Interfacial equilibrium during a first-order phase transformation in solids. J Chem Phys 1986;84(9):5108–21. http://dx.doi.org/10.1063/1.450664.

[87] Hillert M. Phase equilibria, phase diagrams and phase transformations: Their thermodynamic basis. 2. ed., repr ed.. Cambridge: Cambridge University Press; 2009.

[88] Andersson J-O, Helander T, Höglund L, Shi P, Sundman B. Thermo-Calc & DICTRA, computational tools for materials science. Calphad 2002;26(2):273–312. http://dx.doi.org/10.1016/s0364-5916(02)00037-8.

[89] Fukuhara M, Sanpei A. Elastic moduli and internal friction of low carbon and stainless steels as a function of temperature. ISIJ Int 1993;33(4):508–12. http://dx.doi.org/10.2355/isijinternational.33.508.

[90] Amos PGK, Mushongera LT, Nestler B. Phase-field analysis of volume-diffusion controlled shape-instabilities in metallic systems-I: 2-dimensional plate-like structures. Comput Mater Sci 2018;144:363–73. http://dx.doi.org/10.1016/j.commatsci.2017.12.045.

[91] Noubary KD, Kellner M, Hötzer J, Seiz M, Seifert HJ, Nestler B. Data workflow to incorporate thermodynamic energies from calphad databases into grand-potential-based phase-field models. J Mater Sci 2021;56(20):11932–52. http://dx.doi.org/10.1007/s10853-021-06033-7.

[92] Hötzer J, Reiter A, Hierl H, Steinmetz P, Selzer M, Nestler B. The parallel multi-physics phase-field framework Pace3D. J Comput Sci 2018;26:1–12. http://dx.doi.org/10.1016/j.jocs.2018.02.011.

[93] Li S, Sauer R, Wang G. A circular inclusion in a finite domain I. The Dirichlet-eshelby problem. Acta Mech 2005;179(1–2):67–90. http://dx.doi.org/10.1007/s00707-005-0234-2.

[94] Fischer FD, Zickler GA, Svoboda J. Elastic stress–strain analysis of an infinite cylindrical inclusion with eigenstrain. Arch Appl Mech 2018;88(3):453–60. http://dx.doi.org/10.1007/s00419-017-1318-x.

[95] Eshelby JD. The determination of the elastic field of an ellipsoidal inclusion, and related problems. Proc R Soc Lond Ser A. Math Phys Sci 1957;241(1226):376–96. http://dx.doi.org/10.1098/rspa.1957.0133.

[96] Eshelby JD. The elastic field outside an ellipsoidal inclusion. Proc R Soc Lond Ser A. Math Phys Sci 1959;252(1271):561–9. http://dx.doi.org/10.1098/rspa.1959.0173.

[97] Mura T. Micromechanics of defects in solids. Dordrecht: M. Nijhoff; 1987, p. 587.

[98] Hakala RW. A brief derivation of the lever law. J Chem Educ 1952;29(9):453. http://dx.doi.org/10.1021/ed029p453.

[99] Bertram A. Elasticity and plasticity of large deformations. Cham: Springer; 2021, http://dx.doi.org/10.1007/978-3-030-72328-6.

[100] Bertram A, Glüge R. Solid mechanics. Cham: Springer; 2015, http://dx.doi.org/10.1007/978-3-319-19566-7.

[101] Eiken J. Numerical solution of the phase-field equation with minimized discretization error. IOP Conf Ser: Mater Sci Eng 2012;33:012105. http://dx.doi.org/10.1088/1757-899x/33/1/012105.